Contact Thermal Lithography

by

Aaron Jerome Schmidt

Submitted to the Department of Mechanical Engineering
in partial fulfillment of the requirements for the degree of

Master of Science in Mechanical Engineering

at the

MASSACHUSETTS INSTITUTE OF TECHNOLOGY

May 2004

© Massachusetts Institute of Technology 2004. All rights reserved.

Author

Department of Mechanical Engineering
May 18, 2004

Certified by.........   ....
Gang Chen
Professor
Thesis Supervisor

Accepted by ....
Ain Sonin
Chairman, Department Committee on Graduate Students

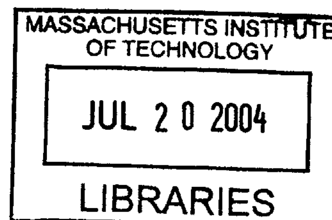
MASSACHUSETTS INSTITUTE OF TECHNOLOGY
JUL 2 0 2004
LIBRARIES

BARKER

Contact Thermal Lithography

by

Aaron Jerome Schmidt

Submitted to the Department of Mechanical Engineering
on May 18, 2004, in partial fulfillment of the
requirements for the degree of
Master of Science in Mechanical Engineering

Abstract

Contact thermal lithography is a method for fabricating microscale patterns using heat transfer. In contrast to photolithography, where the minimum achievable feature size is proportional to the wavelength of light used in the exposure process, thermal lithography is limited by a thermal diffusion length scale and the geometry of the situation. In this thesis the basic principles of thermal lithography are presented. A traditional chrome-glass photomask is brought into contact with a wafer coated with a thermally sensitive polymer. The mask-wafer combination is flashed briefly with high intensity light, causing the chrome features heat up and conduct heat locally to the polymer, transferring a pattern. Analytic and finite element models are presented to analyze the heating process and select appropriate geometries and heating times. In addition, an experimental version of a contact thermal lithography system has been constructed and tested. Early results from this system are presented, along with plans for future development.

Thesis Supervisor: Gang Chen
Title: Professor

Acknowledgments

This work could not have been completed without the support of many people. First among these is my advisor, Professor Gang Chen. His guidance, wisdom and good humor made the entire process enjoyable. Kurt Broderick in EML was instrumental in the fabrication and testing of samples. He always took time to share his expertise and offer advice. Dr. James Goodberlet provided plans for the vacuum sample holder and shared his knowledge on contact lithography, and Dr. Xiaoyuan Chen taught me some basic optics and kept our laser running smoothly. I would also like to thank all the members of the Nanoengineering Group, who were always willing to listen to ideas and give back new ones.

I am indebted to my family for their unconditional support in all my endeavors, and to Jennifer Yu for keeping me well rounded. Finally, thanks to the Department of Defense for their generous financial support.

Contents

1 Introduction **11**

1.1 Background 11

1.2 Contact Thermal Lithography 15

2 Modeling **17**

2.1 Basic Approach 17

2.2 Optical Modeling 18

2.3 Thermal Modeling 24

2.3.1 Limitations and Assumptions 24

2.3.2 Analytic Solutions 26

2.3.3 Numerical Solutions 29

3 Experimental Setup **39**

3.1 Optics 40

3.2 Wafer Stage 44

3.3 Materials Selection 47

4 Method and Results **49**

4.1 The CTL Process Flow 49

4.2 Results 51

5 Discussion and Conclusion **55**

5.1 Short Term Goals 55

5.2 Long Term Goals and Commercial Potential 57

5.3 Conclusion 58

A Material Properties **59**

A.1 Optical Properties 59

A.2 Thermal Properties 62

B LabVIEW Software **63**

List of Figures

1-1 Projection photolithography 12
1-2 Nano Imprint Lithography 13
1-3 Contact Thermal Lithography geometry 15
1-4 The CTL process flow 16

2-1 Reflection and absorption by a photomask 19
2-2 Reflectivity of the mask structure for three metals 21
2-3 The 95% absorption length of 3 metals 22
2-4 Mask with a thin metal layer 23
2-5 Optical properties for a thin metal layer 23
2-6 Simple 1D representation of the conduction problem 26
2-7 Thermal capacity of the metal layer 28
2-8 Temperature in the polymer layer 29
2-9 2D model used in ADINA finite element analysis 31
2-10 A typical ADINA mesh 32
2-11 A temperature contour plot 33
2-12 Time evolution of the lateral temperature profile 34
2-13 Lateral temperature profile along the resist top surface 35
2-14 2D model with reduced dimensions 36
2-15 Lateral temperature profile for the reduced model 36

3-1 Schematic of the basic CTL system 40
3-2 Optical pulse generation system 41
3-3 Pulse length as a function of angular step size 42

3-4 Beam profiling apparatus 43
3-5 A typical beam profile 43
3-6 Vacuum wafer fixture 45
3-7 Groove cut on the bottom plate 45
3-8 Vacuum wafer with top seal in place. 46
3-9 Newton's rings between the mask and wafer 46
3-10 Vacuum wafer assembly mounted on a motion stage 47

4-1 The exposure procedure 51
4-2 Early test results 52
4-3 Resist regions torn by adhesion 53
4-4 Images of the photomasks following laser exposure 53
4-5 The boundary between a region of solid Cr and clear glass 54

B-1 LabVIEW interface for the CTL system. 64

Chapter 1

Introduction

1.1 Background

Photolithography is the industry-standard method by which microelectronic circuits and other small-scale devices are produced. The basic procedure, depicted in Figure 1-1, is simple: light is projected through a mask onto a wafer coated with a polymer film known as photoresist. The light causes a chemical change in the exposed regions of the resist, and subsequent development with an appropriate solvent washes away either the exposed or unexposed regions, depending on the resist chemistry. The remaining pattern is then used as a mask to protect the underlying area. The minimum feature size this method can achieve is proportional to the wavelength of light employed in the exposure process:

$$W_{min} = \frac{k\lambda}{\mathrm{NA}} \tag{1.1}$$

Here λ is the wavelength, NA is the numerical aperture of the exposure system, and k is a parameter of the system.

Photolithography can be done in contact mode or projection mode. In contact mode, the mask is placed directly on the wafer, while in projection mode there is a gap between the two. Projection photolithography is the current industry standard. It allows for greater throughput, simpler mask alignment and optical reduction of the mask features on the wafer. However, contact lithography has potential advantages

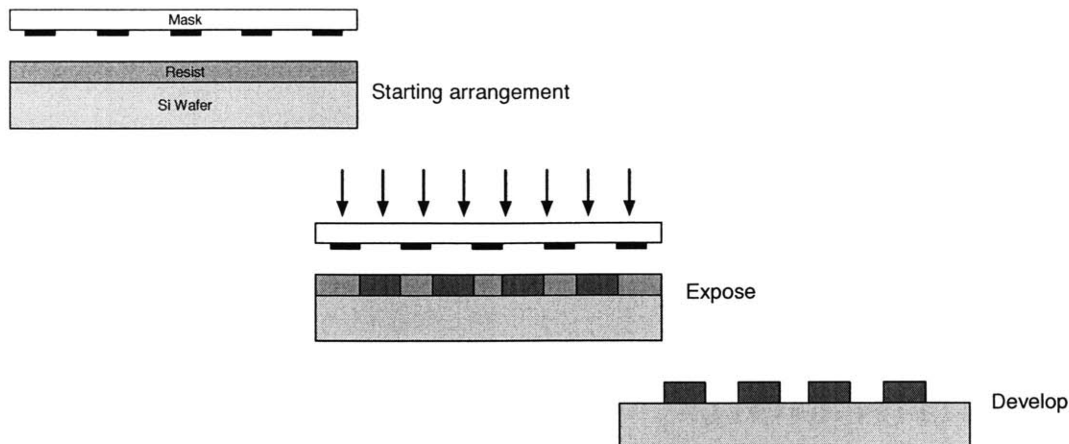

Figure 1-1: Projection photolithography. Light shines through a mask and exposes photoresist. Development transfers the mask pattern.

resulting from near-field optical effects and is also being actively developed.[1]

In an ongoing effort to fit more features into smaller spaces, engineers have been improving each term of equation 1.1. The parameter k depends on the exposure tool, the mask, and properties of the photoresist. Through advances in exposure optics, phase-shifting mask features and resist chemistries, k has been reduced to around 0.4 in the best cases. There is little room left for improvement, however, because for spatially incoherent illumination k has a theoretical minimum of 0.25. The numerical aperture of high-performance lithography systems is in the neighborhood of 0.6, and techniques such as liquid immersion may boost this number closer to one. Such techniques will also increase the cost and complexity of exposure systems. Finally, the semiconductor industry has been steadily decreasing exposure wavelength. The most current technology uses 193 nm light, and a future shift to 157 nm is expected. Unfortunately, each advance requires new and expensive lens technology utilizing exotic materials such as CaF_2.

The cumulative effect of all these efforts has been that the number of features on a semiconductor chip has roughly doubled every 18 months for the past three decades. Unfortunately, this progress has been accompanied by exponentially increasing capital costs.[2] Individual fabrication tools, such as lithography steppers, have reached tens of millions of dollars, and complete modern fabrication facilities require investments

of several billion dollars. If this trend continues, economic constraints will seriously limit lithographic progress.

Fortunately, there are a number of alternative lithographic techniques that have emerged in recent years. Common to many of these techniques is that the resolution has been uncoupled from an exposure wavelength. This frees them from many challenges facing traditional lithography and provides hope for avoiding escalating capital costs. One of the best known alternative lithographies is known as Nano Imprint Lithography (NIL).[3] NIL has produced features as fine as 10 nm and has spawned a number of similar techniques for pattern transfer.[4]

Conceptually, NIL is simple. A rigid template consisting of raised features is pressed into a polymer resist, creating an imprint. Subsequent etching transfers this imprint to the substrate below. The basic process is depicted in Figure 1-2. The templates are typically fabricated on quartz substrates using conventional electron beam lithography, which has excellent resolution but poor throughput. The imprinting layer is normally polymethylmethacrylate (PMMA) which has been heated above its glass transition temperature of roughly 105 °C, and the required imprint pressure is between 10 and 100 MPa.

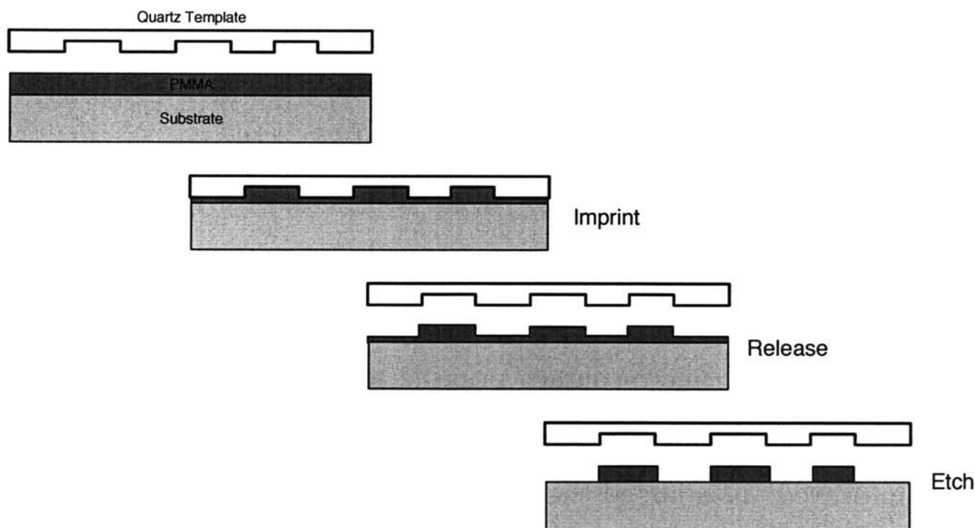

Figure 1-2: Nano Imprint Lithography (NIL). A rigid template is pressed into a maleable polymer layer, creating an imprint. Etching removes the depressed regions, leaving behind a pattern that serves as a mask for future processes.

NIL has had success reproducing a wide variety of patterns and even some functional devices.[5] However, it has important limitations. Certain types of patterns are difficult to imprint, particularly isolated recessed features. The high pressures involved require large forces for even moderately sized templates, and the pressures can deform the underlying substrate, posing a challenge for the fabrication of multi-layer structures. In addition, a planarization step is required between layers in multilevel structures. Finally, issues such as thermal expansion and layer-to-layer alignment limit the ability to produce complex multi-template devices.[6]

Variants on the NIL process have attempted to address some of these limitations. One such variant is Step and Flash Imprint Lithography (SFIL).[7] In SFIL, a low viscosity, photopolymerizable polymer is dispensed onto a wafer. A template is then pressed onto the wafer, displacing the polymer and causing it to fill the template relief patterns. With the template still in contact, the polymer is cured with UV light. The template is then removed, leaving behind the patterned and cured polymer.

Like NIL, SFIL appears only to be limited by the template resolution, and features down to 20 nm have been reproduced.[8] However, pressures less than 5 MPa are needed to fill typical patterns.[9] This greatly reduces the required imprinting force and the risk of deformation. SFIL also does not require high temperatures, minimizing thermal expansion. A key challenge for SFIL is imprint thickness and uniformity over large substrate areas. This requires great control in the way droplets of liquid photopolymer are dispensed over the surface. SFIL also must contend with some of the same issues as NIL, including multilayer alignment and planarization.

There are numerous other alternative lithographies being developed. These include laser-assisted NIL, micro-contact printing and various scanning probe direct write techniques.[6] Each has its own strengths and weaknesses, and most are continually being improved. It is hoped that one or a combination of such new techniques will be able to meet future micro- and nano-fabrication requirements.

1.2 Contact Thermal Lithography

Contact Thermal Lithography (CTL) is a new approach to fabrication. It incorporates aspects of contact photolithography and NIL but is distinct from both. The concept is straightforward: a mask consisting of metal patterned on glass is brought into contact with a wafer that has been coated with a thermally sensitive polymer referred to as thermoresist. The combination is flashed briefly with a high intensity laser of visible wavelength. The patterned metal features are strongly absorbing and rapidly heat up, while the optically transparent glass and polymer do not. Due to the short flash duration, the metal conducts heats only to the directly contacted polymer, causing local crosslinking. After the mask is removed the wafer is developed in an appropriate solution, leaving behind only the crosslinked regions. Because the underlying wafer may be optically absorbing, a thermal buffer layer such as SiO_2 is required between the wafer and the thermoresist. The mask-wafer arrangement is depicted in Figure 1-3 and a representation of the process flow is shown in Figure 1-4.

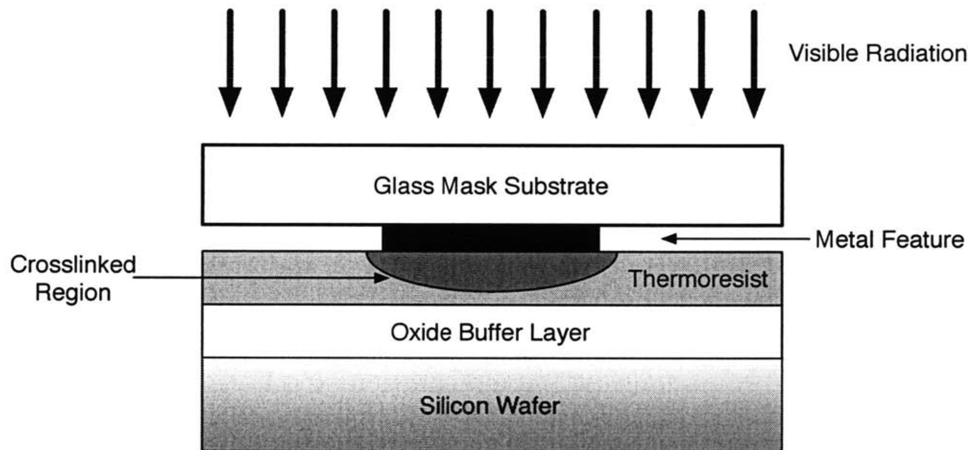

Figure 1-3: Basic Contact Thermal Lithography (CTL) geometry. Radiation incident on the mask heats up the metal feature. The heat is conducted to the underlying polymer, causing crosslinking.

Unlike NIL and SFIL, contact thermal lithography requires only enough pressure to ensure intimate contact between the mask and wafer. In addition, it can reproduce truly arbitrary features without concern for the flowing and redistribution of an im-

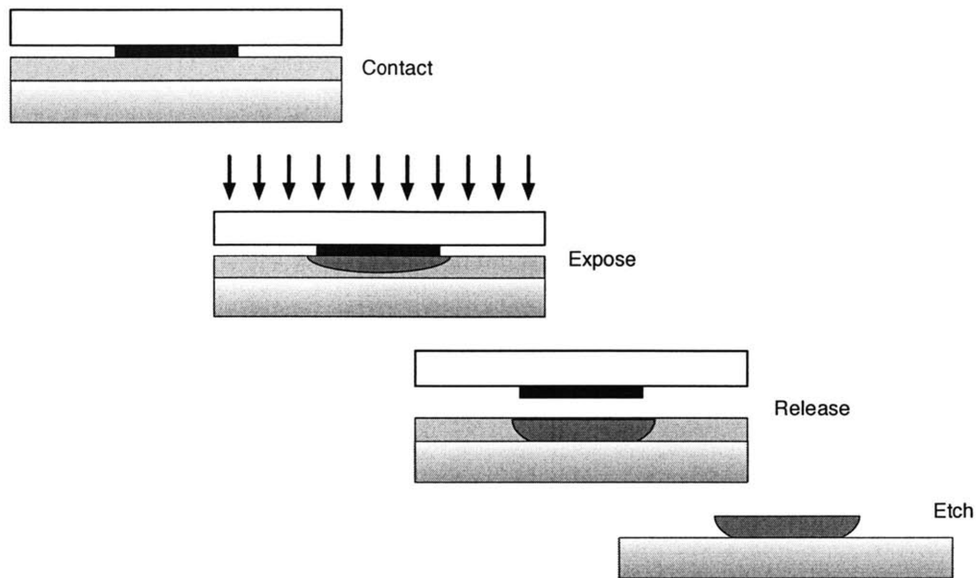

Figure 1-4: The CTL process flow. The SiO_2 buffer layer has been omitted for clarity.

printing layer. It also promises high throughput due to the extremely short heat-cool cycle. Like all contact lithography techniques CTL faces challenges with regard to surface planarization and multi-layer alignment, but these issues are being dealt with by numerous research and commercial groups.[6]

The goal of this thesis is to demonstrate the feasibility of contact thermal lithography. Criteria for the selection of mask and resist materials are discussed, along with the fundamental limits imposed by the optical and thermal characteristics of the situation. These details are covered in the next chapter. Chapter 3 describes in detail a simple, proof-of-concept implementation of a CTL system that has been constructed. This system is built around easily obtainable materials and photomasks. As a result, the target resolution is on the order of microns instead of nanometers. However, the early implementation highlights several potential issues with a CTL system and has the potential to be extended to smaller feature reproduction. The experimental procedure and some results produced by this system are presented in Chapter 4, including a discussion of a number of difficulties that were encountered. Chapter 5 summarizes the research and examines future challenges and opportunities for this new technology.

Chapter 2

Modeling

2.1 Basic Approach

Modeling CTL involves optical, thermal and materials problems. Here the focus is primarily on the optical and thermal problems; a theoretical treatment of the materials issues is left for future work.

The optical problem is fairly simple. High intensity, monochromatic light impinges on a stack of materials at normal incidence. The stack consists of some type of glass, a thin metallic layer, and a thermally sensitive polymer. Given the intensity and wavelength of the source, the goal is to predict the rate at which energy is absorbed by the metallic layer. Using electromagnetic theory, the portions of energy that are reflected, absorbed and transmitted are calculated.

Once the conversion rate between optical and thermal energy is known, the thermal behavior of the system can be modeled. The dominant mode of heat transfer from the metal to the polymer is conduction. The transient heat transfer characteristics are estimated with a simple 1-D model. A finite element model is used to make a more precise 2-D estimate of the temperature evolution in the polymer resist layer.

For a given resist material, there will be a threshold temperature above which polymer crosslinking occurs. The transient heating characteristics of the polymer are used to deduce the appropriate optical intensity and exposure time necessary to cure the resist through its thickness. These parameters will depend on the specific material

properties of the mask and the resist, as well as the thickness of the resist layer.

2.2 Optical Modeling

The purpose of the photomask in normal photolithography is to reduce optical intensity to zero in the masked areas. In thermal lithography, however, the ideal mask absorbs the maximum optical energy, regardless of the amount of transmitted light. This distinction is explored in this section. The simplest case, in which the metal layer is sufficiently thick to absorb all incoming light, is examined first. It is the case that most closely matches the experimental setup, and the analysis used is general enough to then be easily extended to the thin-layer case.

Figure 2-1 shows a model of the mask in cross section. Monochromatic light at normal incidence strikes the glass surface with intensity I. Some portion R is reflected back toward the source, and the remainder T is ultimately absorbed by the metallic layer. It is necessary to calculate the fraction of absorbed energy in order to determine the heating rate in the metal. It is assumed that the metal layer is sufficiently thick to absorb the transmitted radiation. This assumption will be justified later.

The optical properties of layered structures have been studied extensively. If the optical properties of the constituent materials are known, it is a simple matter to calculate the overall properties of the layered structure. In many situations, it is difficult to calculate the reflectivity and transmissivity of materials due to the scattering of light by microscopic peaks and valleys on the surface. However, in the case when the surface is optically smooth (when surface variations are smaller than the optical wavelength), the reflectivity and transmissivity can be found using the standard Fresnel coefficients. Under the condition of normal incidence, the reflectivity is given by

$$R = \left| \frac{N_2 - N_1}{N_2 + N_1} \right|^2 \tag{2.1}$$

where N_1 and N_2 are the indices of refraction of materials 1 and 2, respectively. The result holds for absorbing materials, in which case N will be have an imaginary part.

This result, valid for a single interface, can be extended to a series of interfaces.

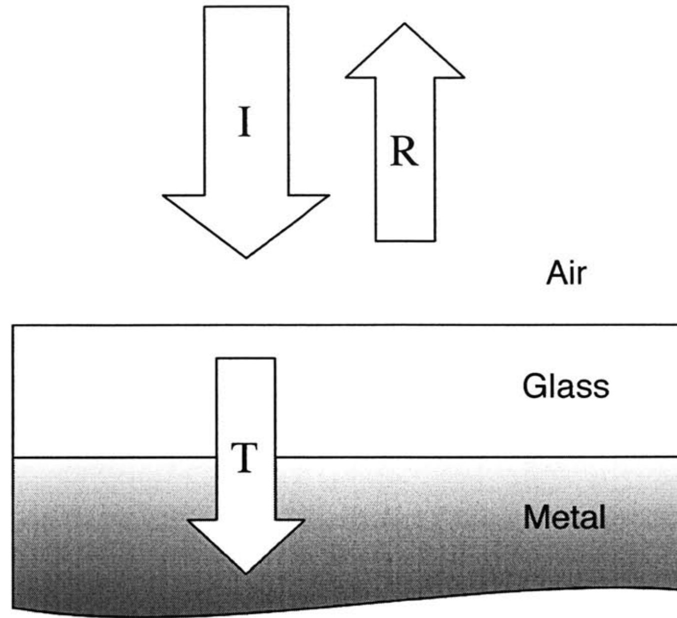

Figure 2-1: Reflection and absorption by a photomask. A fraction of the incoming intensity is reflected by the Air-Glass and Glass-Metal interfaces, and the rest is transmitted into and absorbed by the metal layer.

There are two approaches to this problem, ray tracing and wave optics. The ray tracing approach is simpler. At each interface the reflected and transmitted intensities are tabulated, and the endless internal reflections are summed up simply in a geometric series, giving the net properties for the stack. This approach neglects any phase information carried by the electromagnetic waves. If the individual layers are thick compared to the wavelength and the coherence length of the source, then the approximation is good. As the layer size shrinks, however, interference effects will alter the results.

The alternative approach is to solve the full set of electromagnetic equations inside each layer under the constraint that the fields match correctly at the interfaces. This can be done in matrix format, in an approach known as the transfer matrix method.[10] Equation (2.2) gives the reflectivity for a layered structure containing m layers:

$$R = \left| \frac{(m_{11} + m_{12}p_{m+1})p_0 - (m_{21} + m_{22}p_{m+1})}{(m_{11} + m_{12}p_{m+1})p_0 + (m_{21} + m_{22}p_{m+1})} \right|^2 \tag{2.2}$$

The subscripts 0 and $m+1$ indicate the media on either side of the layered structure

and the elements m_{ij} are taken from the overall transfer matrix M given by

$$M = \prod_{j=1}^{m} M_j = \begin{bmatrix} m_{11} & m_{12} \\ m_{21} & m_{22} \end{bmatrix}$$

The individual transfer matrices M_j are given by

$$M_j = \begin{bmatrix} \cos\phi_j & -\frac{i}{p_j}\sin\phi_j \\ -ip_j\sin\phi_j & \cos\phi_j \end{bmatrix}$$

where

$$\begin{aligned} \phi_j &= \frac{\omega N_j d_j \cos\theta_J}{c_o} \\ p_{j,TM} &= \sqrt{\frac{\mu_j}{\epsilon_j}}\cos\theta_j \\ p_{j,TE} &= \sqrt{\frac{\epsilon_j}{\mu_j}}\cos\theta_j \end{aligned}$$

Here ω is the radiation frequency, N_j and d_j are the index of refraction and thickness of the j_{th} layer, θ_j is the propagation direction and ϵ_j and μ_j are the electric permittivity and magnetic permeability of the j_{th} layer. c_0 is the speed of light in vacuum and the subscripts TM and TE denote transverse magnetic and transverse electric polarizations. For normal incidence, all $\theta_j = 0$ and the TM and TE cases reduce to the same result.

Equation (2.2) was used to calculate the reflectivity of the structure shown in Figure 2-1. Although the photomask structure is much thicker than optical wavelengths, the coherence length of a laser can be meters or kilometers long and equation (2.2) will capture the resulting interference effects. Of course, the surfaces still must be parallel and optically smooth or the results will not be accurate. The mask substrate is assumed to be fused silica, with a thickness of 500 μm. The results are shown in Figure 2-2 as a function of wavelength for three common metals, Cr, Al and Fe. The reflectivity is shown only at some common laser wavelengths. The optical properties of the various materials used in calculation are given in Appendix A.

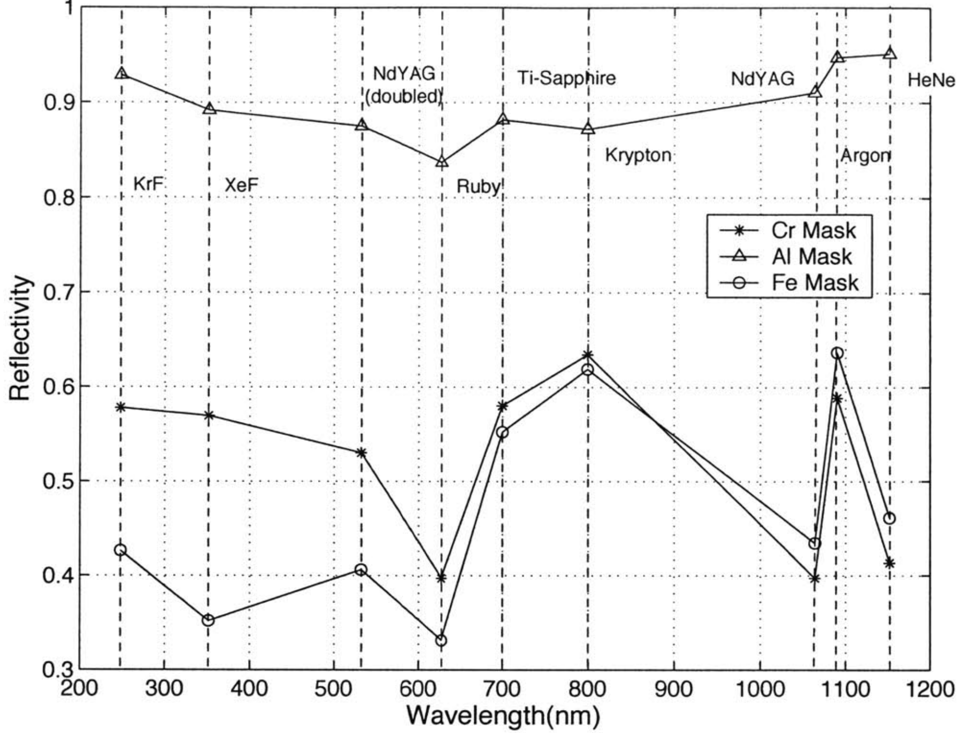

Figure 2-2: Reflectivity of the mask structure for three types of metal layer. The results are calculated at some common laser wavelengths.

In the thick-film case, the majority of the light transmitted into the metallic layer should be absorbed and converted to heat, so that the volumetric heating rate $\dot{Q} = I(1 - R)/t$ where t is the thickness of the metal. This is ensured by giving the layer adequate thickness. The rate at which intensity decays inside an absorbing material is given by

$$I_\lambda = I_\lambda(0) \exp \frac{-4\pi\kappa(\lambda)z}{\lambda} \tag{2.3}$$

Here, $I_\lambda(0)$ is the initial intensity, z is the distance into the material, and κ is the imaginary portion of the complex index of refraction $\overline{N} = N - i\kappa$. Using the known optical properties listed in Appendix A, the thickness required to reduce a propagating wave to 5% of its original intensity is plotted for three metals in Figure 2-3. This result serves as a guide for the necessary metal thickness depending on the exposure wavelength.

It is possible to achieve significantly higher absorption than the case of a very

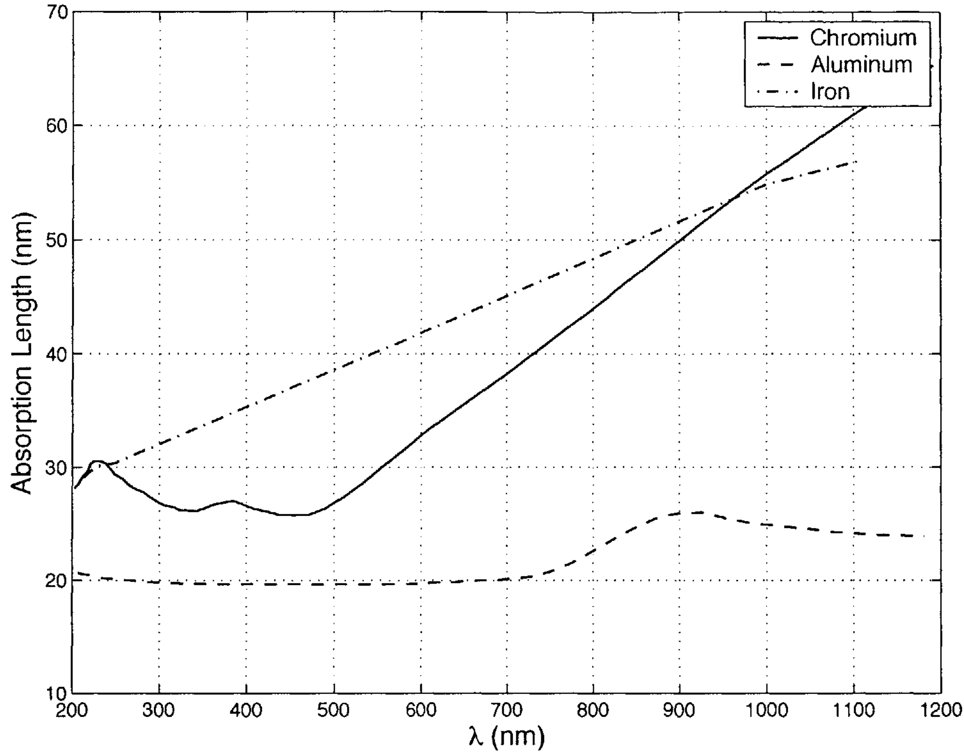

Figure 2-3: The 95% absorption length plotted as a function of wavelength for 3 metals.

thick metal layer. If the mask is not required to reduce optical transmittance to zero, wave interference effects may enhance the absorbed optical energy. Consider for example the situation depicted in Figure 2-4, where the transmitted energy may be significant. For a given wavelength λ, the reflectivity, transmissivity and absorptivity will all be functions of the metal layer thickness.

To illustrate this, the absorptivity of a thin film of Cr was calculated using equation (2.2). The results are plotted in Figure 2-5. The particular wavelength chosen was 532 nm and the thickness t was varied between zero and 70 nm. At a metal thickness of 8.5 nm, the absorptivity of the layer has a value 25% higher than that predicted for an infinitely thick metal layer. As the thickness t increases, the optical properties approach those of the thick-layer case and the reflectivity is equal to that shown in Figure 2-2 for a Cr film at 532 nm.

Although optimizing the film thickness for maximum absorptivity is desirable,

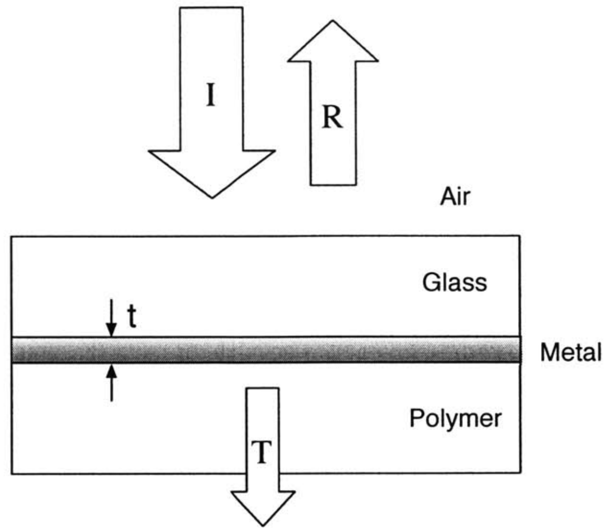

Figure 2-4: A mask with a thin metal layer in contact with a polymer resist. Although the transmitted intensity is not reduced to zero, absorption may be higher than the case shown in Figure 2-1

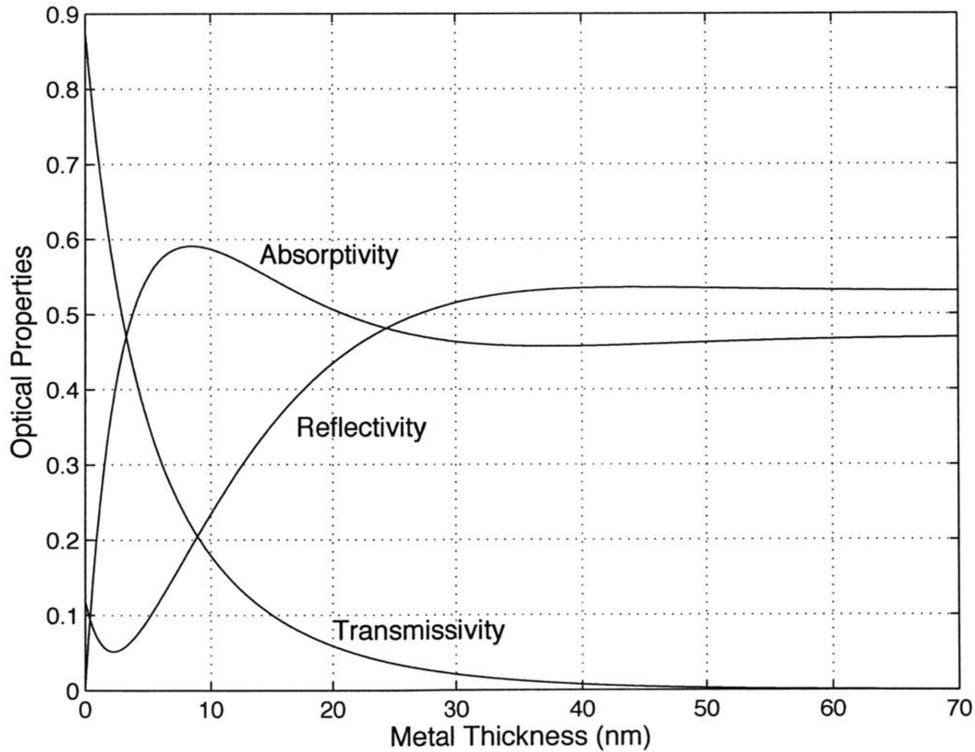

Figure 2-5: Optical properties for the structure shown in Figure 2-4. At a metal thickness of 8.5 nm, the absorptivity of the film reaches its maximum value.

practical concerns may impose additional constraints. The durability of the metal features may be compromised as the layer thickness shrinks. In addition, many coating processes require a minimum thickness to ensure even coverage. Depending on the metal and coating process being used, these effects must also be considered.

2.3 Thermal Modeling

2.3.1 Limitations and Assumptions

Transient heat conduction in isotropic bulk solids is governed by the diffusion equation

$$\rho c \frac{\partial T}{\partial t} = \dot{q} + k\nabla^2 T \tag{2.4}$$

where T is temperature, ρ the density, c the specific heat capacity, $\dot{q}$ the volumetric heat generation term, and k the thermal conductivity. Solutions to this equation will comprise the majority of the analysis presented here. There are, however, limits to equation (2.4)'s applicability, particularly when the characteristic dimensions of the problem are very small or when molecular orientation results in anisotropies. It is necessary to explore these limits before proceeding.

In dielectric (non-conducting) solids, energy is primarily carried by quantized lattice vibrations known as phonons. Energy transport can accurately be modeled as a diffusion process when the distance a phonon travels between collisions with other phonons is small compared to the dimensions of the structure. This inter-collision distance is referred to as the mean free path. In addition, the intrinsic quantum wavelength of the carrier itself should be smaller than the dimensions of the structure. If either of these conditions is not satisfied, energy transport can be modeled using ballistic transport theory or, if necessary, quantum mechanics.[11]

The mean free path $l(T)$ for amorphous dielectrics can be approximated as

$$l(T) = \frac{3K(T)}{C(T)v} \tag{2.5}$$

where K is the thermal conductivity, v is the average phonon velocity and C is the volumetric heat capacity.[12] Using this method, the mean free path has been calculated for a number amorphous solids. For typical materials such as PMMA or amorphous SiO_2, $l < 10$ Å for $T > 100$ K.[12] At 300 K, a typical phonon wavelength is also on the order of 10 Å.[11] Thus, for amorphous structures with dimensions of 10 nm or more the diffusion model is adequate and equation (2.4) applies.

Isotropy is more difficult to justify. Polymers are often composed of very long and complex molecules, and when the polymer is applied in a thin film the molecules tend to align themselves in a preferred orientation. This can potentially impact both thermal and mechanical properties. Unfortunately, there is no simple way to predict whether or not anisotropy will occur. When a polymer is drawn in a given direction, thermal conductivity tends to increase in the drawn direction and decrease in the perpendicular direction. Depending on the polymer and the degree of drawing, departure from the bulk isotropic conductivity may be anywhere from 1% to 50%.[12]

The thermal properties of very few polymers have been studied in a thin film configuration. Those studies that have been done do not indicate a simple pattern. For example, the ratio of in-plane to out-of-plane thermal conductivity for PMDA-ODA polyimide films is expected to asymptotically approach a value of 10 as film thickness decreases below 1 μm.[13] On the other hand, similar work with PMMA has shown no appreciable anisotropy.[14] In the latter case, however, thermal conductivity was shown to be roughly 2/3 the bulk value. To complicate matters further, thermal conductivity is a function of both temperature and the degree of crosslinking in the polymer.

Therefore, to accurately asses the thermal characteristics of a given polymer in a thin film configuration, it is necessary to perform a detailed study of that particular polymer under conditions similar to those of the actual exposure process. For the sake of simplicity, it is assumed here that the thermoresist film has isotropic material properties similar to those of PMMA. The following analysis should be modified to account for more complex material behavior if data is available.

2.3.2 Analytic Solutions

Keeping the above limitations in mind, equation (2.4) is used to model the thermal behavior of a CTL system. In most cases it is not possible to obtain analytic solutions to this equation. However, exact solutions for simple 1D situations are available, and these can give insight into more complex problems.

Figure 2-6 depicts a simplified 1D model of the mask-wafer arrangement. It consists of a heat-generating layer sandwiched between two different materials, representing the glass-metal-polymer arrangement of CTL. This model will not yield any insight into lateral heat conduction and edge effects, but will give an indication of the time and temperature scales involved in the problem.

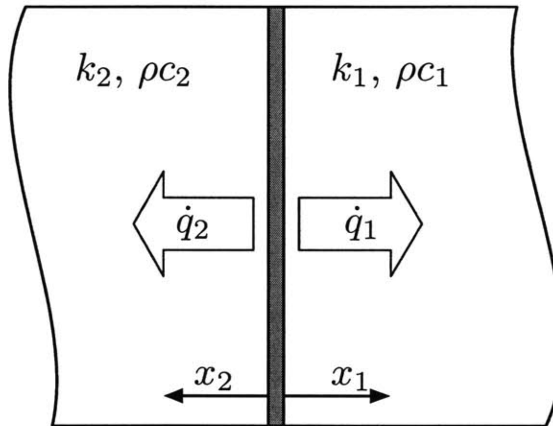

Figure 2-6: Simple 1D representation of the conduction problem

A solution for this case can be built on the solution to an even simpler problem - a semi-infinite surface subjected to constant heat flux. For such a situation, the solution is given by [15]

$$T_{x'}(t) = T_i + \frac{q_s}{k} \int_{x'}^{\infty} \text{ercf}(x/2\sqrt{\alpha t})dx \tag{2.6}$$

Here $T_{x'}(t)$ is the temperature at distance x' from the surface of the body at time t, T_i is the initial temperature of the body, q_s is the heat flux at the surface, α is the thermal diffusivity of the material and erfc is the complementary error function. At

the surface where $x' = 0$, this reduces to

$$T_s(t) = T_i + 2\frac{q_s}{k}\sqrt{\frac{\alpha t}{\pi}} \quad (2.7)$$

In order to apply equation (2.6) to the model shown in Figure 2-6, two conditions must be satisfied: the energy that goes into heating the metal absorber must be negligible compared to the flux into the two semi-infinite bodies, and the ratio of the heat fluxes into the two semi-infinite bodies must be constant. It is simplest to assume the former condition holds and prove the latter, and then verify that the assumption was valid.

Assuming both surfaces have the same initial temperature and that there is no temperature gradient across the thin metal layer, both bodies must have the same surface temperature. Then,

$$\frac{q_1}{k_1}\sqrt{\frac{\alpha_1 t}{\pi}} = \frac{q_2}{k_2}\sqrt{\frac{\alpha_2 t}{\pi}}$$

The ratio q_1/q_2 is indeed constant and is given by

$$\gamma = \frac{q_1}{q_2} = \frac{k_1}{k_2}\sqrt{\frac{\alpha_2}{\alpha_1}} \quad (2.8)$$

Thus each side of the model can be treated as an isolated case that can be solved with equation (2.6) using a value of q_s that has been reduced by the appropriate fraction.

It is now straightforward to verify that the metal layer absorbs a negligible amount of energy. This condition is expressed as

$$C\frac{dT}{dt} \ll q_1 + q_2$$

where C is the heat capacity of the metal layer. Using equations (2.7) and (2.8), this becomes

$$\frac{C}{k_1}\left(\frac{\gamma}{\gamma+1}\right)\sqrt{\frac{\alpha_1}{\pi t}} = \beta \ll 1 \quad (2.9)$$

Figure 2-7 plots the quantity β as a function of time using representative properties. The metal layer is Cr and is 50 nm thick. Material 1 is a typical polymer and

material 2 is glass. Depending on the material properties, γ^{-1} ranges between 3 and 15; the value used here was 5. As the figure shows, the thermal capacity of the metal layer will have an impact only for the very early stage of heating. Thus solutions ignoring this thermal capacity will overestimate the flux into the semi-infinite bodies for the first microsecond of heating but will become increasingly accurate as time progresses.

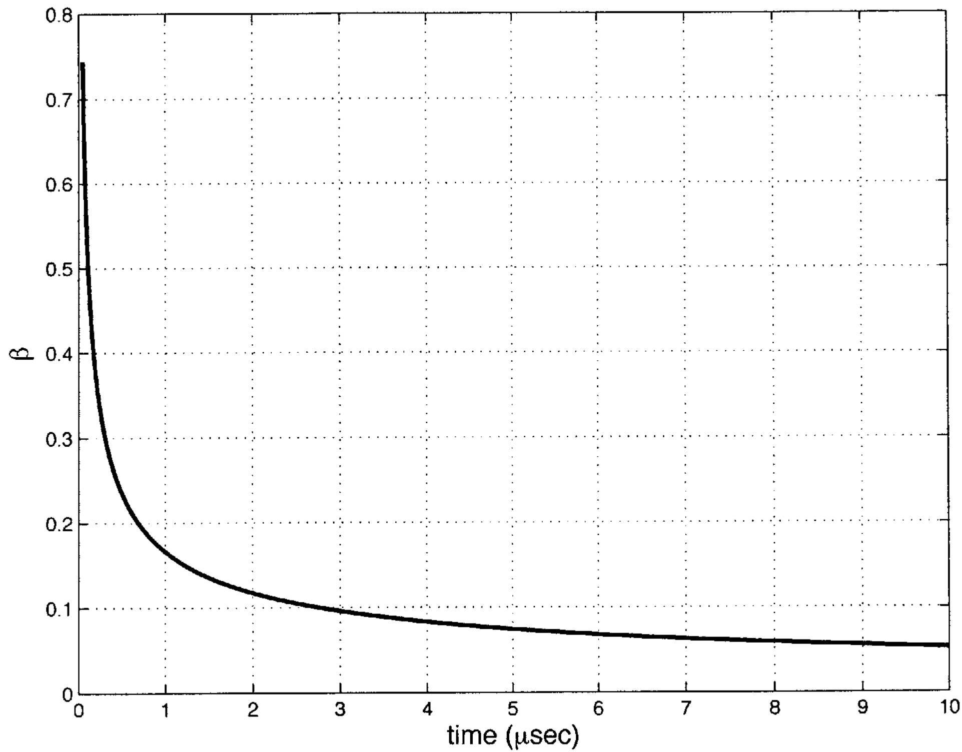

Figure 2-7: The quantity β plotted against time. The thermal capacity of the metal layer has negligible importance for $\beta \ll 1$

Neglecting the heat capacity of the metal layer, equation (2.6) can now be used to predict the temperature propagation through semi-infinite bodies 1 and 2. In this particular problem, only the temperature distribution in the polymer layer is of interest; this information reveals when and where crosslinking will occur. Figure 2-8 plots the temperature in the polymer layer as a function of time for various positions inside the layer. As in Figure 2-7, representative values for the material properties were used. The transmitted heat flux q_s used was 4.25×10^7 W/m^2, a value in line

with the typical heat fluxes used in the actual experiments. The initial temperature was taken as 20 °C. The thermally sensitive polymers considered in this experiment have crosslinking temperatures between 100 and 200 °C. Figure 2-8 indicates that it should take less than 10 μsec to cure a 500 nm resist layer.

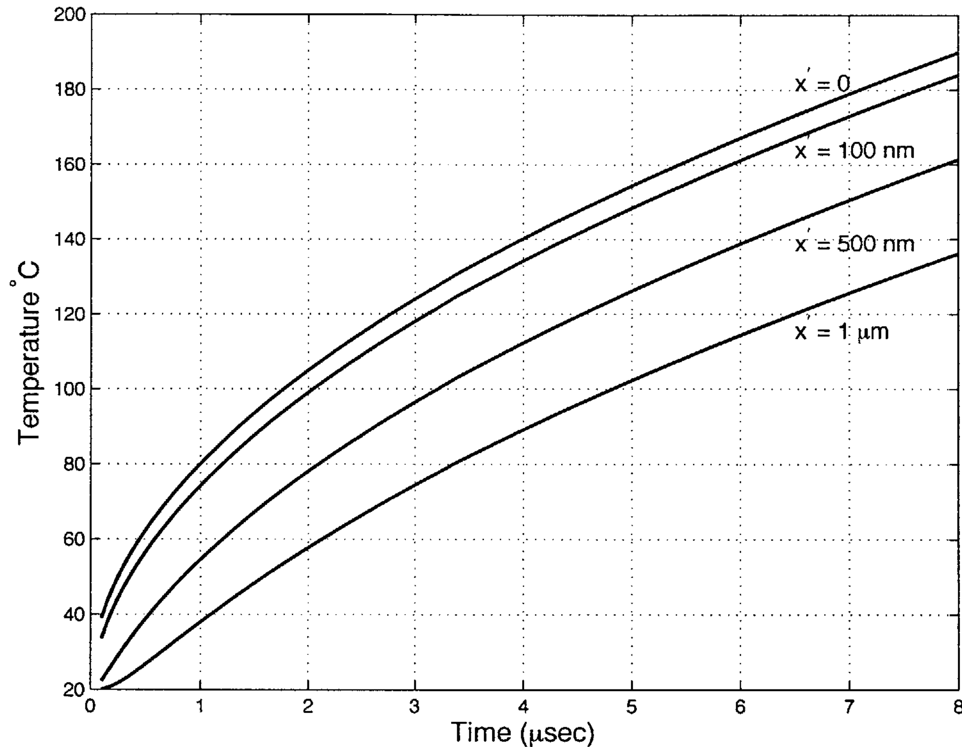

Figure 2-8: Temperature in the polymer layer as a function of time for various positions inside the layer. Typical material properties and a heat flux of 4.25×10^7 W/m^2 were used

2.3.3 Numerical Solutions

The main concern with any lithography system is the minimum feature size that it can reproduce. In optical lithography, this limit is given by equation (1.1). For imprinting techniques, the resolution is limited only by the feature size of the template, which in turn is limited by the resolution of electron beam lithography systems. A reasonable exposure requirement for CTL is that the resist be crosslinked through its entire thickness. Then the resolution will be limited by the amount of lateral heat

conduction in the thermoresist layer during the exposure process. As mentioned in the preceding section, a simple 1D model is insufficient to capture lateral heat flow and edge effects. Therefore, it is necessary to formulate a two-dimensional problem and solve it numerically.

The ADINA Finite Element System was used to construct a 2D representation of the problem and obtain solutions under a variety of loading conditions. A number of models were constructed with different metal dimensions and resist thicknesses. The analysis presented here will focus on a model with dimensions that most closely match those of the experimental apparatus. The results obtained for different geometries are qualitatively similar, and the primary quantitative difference is that smaller mask features and thinner resist layers require shorter heating times to reach target temperatures. Some results illustrating the potential for better resolution are presented at the end of the section. The material properties used in modeling can be found in Appendix A.

The basic model, shown in Figure 2-9, is a sandwich of four layers: glass mask substrate - metal layer - thermal polymer - SiO_2 buffer layer. The top and bottom layers have enough thickness so as not to impact transient heating characteristics of the resist layer. In addition, the model is assumed symmetric about its centerline. This reduces computation time by a factor of two. The dimensions of the metal feature and the resist layer thickness are in agreement with the apparatus discussed in later sections. This allows the simulation results to serve as a guide in choosing the correct laser intensity and exposure duration in the actual experiments.

An adiabatic boundary condition was applied along all outer surfaces and along the axis of symmetry. This is justified because the time scales involved are extremely short and there is no time for appreciable thermal interaction with the surrounding environment. Laser heating was simulated as internal volumetric heat generation within the metal layer. This was accomplished by calculating transmitted optical energy and dividing by the mass of the metal feature.

In order to minimize the numerical precision errors that result from modeling small spatial dimensions and short time scales, the governing equations were nondi-

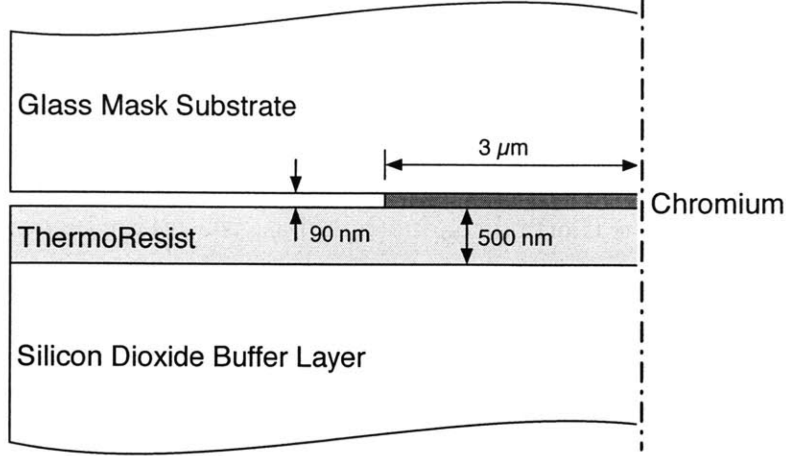

Figure 2-9: 2D model used in ADINA finite element analysis. The dimensions match those from the actual experiment

mensionalized and dimensionless versions of all necessary quantities were input into the ADINA model. In dimensionless form, equation (2.4) becomes:

$$
\begin{aligned}
\text{Material 1:} \quad \frac{\partial \theta}{\partial \zeta} &= \frac{\partial^2 \theta}{\partial \eta^2} + \frac{L_c^2 \dot{q}}{\alpha_1 (\rho c)_1 (T_c - T_i)} \\
\text{Material } n\text{:} \quad \frac{\partial \theta}{\partial \zeta} &= \frac{\alpha_n}{\alpha_1} \frac{\partial^2 \theta}{\partial \eta^2} + \frac{L_c^2 \dot{q}}{\alpha_1 (\rho c)_n (T_c - T_i)}
\end{aligned} \tag{2.10}
$$

where

$$
\begin{aligned}
\theta &\equiv \frac{T - T_i}{T_c - T_i} \\
\zeta &\equiv \frac{\alpha_1 t}{L_c^2} \\
\eta &\equiv \frac{x}{L_c}
\end{aligned}
$$

Here T_i is the initial temperature of the system, T_c is some critical temperature of interest and L_c is a characteristic length of the system. In the present analysis, T_i is taken as 20°C, T_c is 110°C, and L_c is 200 nm.

As indicated in equation (2.10), the diffusion equation for the first material is nondimensionalized using its own physical properties; subsequent materials are nondimensionalized with respect to the first material. This ensures that the relative differ-

ences between the various materials are preserved in the non-dimensional problem. When entering parameters into the finite element model, spatial dimensions were all given in terms of η and time steps in terms of ζ. The heat capacities for all materials were entered as 1 and the thermal conductivity for a material n as α_n/α_1. Finally, the internal heat generation for the metal layer was modified by the appropriate factor shown in equation (2.10).

The model shown in Figure 2-9 was entered into ADINA and discretized into a standard mesh. An image of a typical mesh is shown in Figure 2-10. All results were computed at several mesh sizes to ensure convergence.

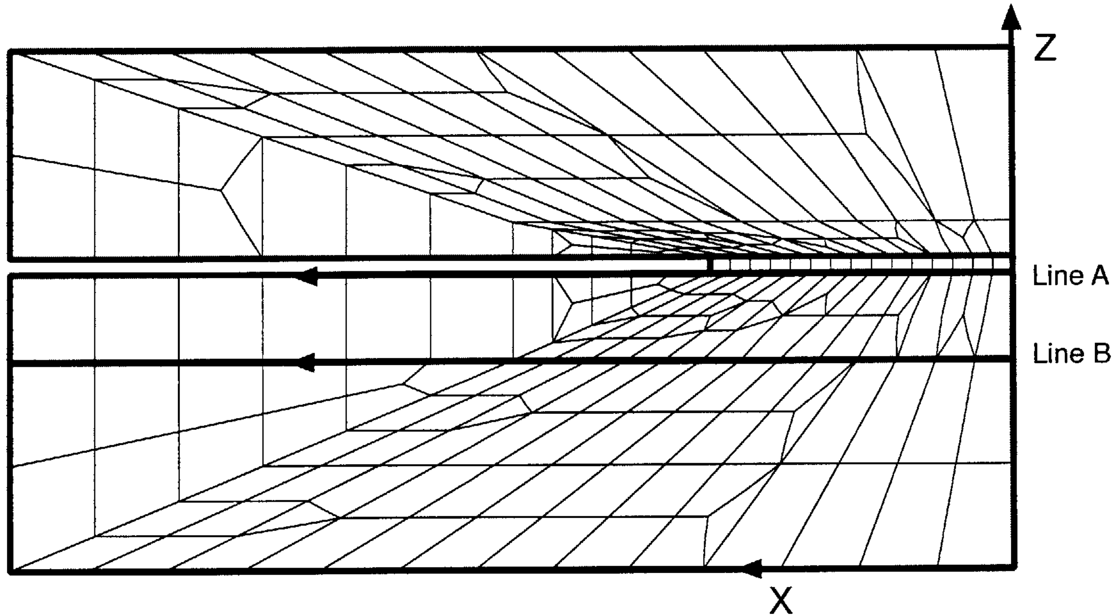

Figure 2-10: A typical mesh used in simulation. Mesh size was varied for each computation to ensure convergence. Values at the nodes along lines A and B are used to study lateral heat flow

The model was subjected to internal heat generation in the metal layer and the resulting temperature contours were observed. As expected, in order to cure the resist through its thickness, there was an amount of lateral temperature spread roughly equal to the thickness of the resist layer. A typical temperature contour plot is shown in Figure 2-11. The scale is in the dimensionless temperature θ. This particular plot is a snapshot taken at $t = 15\mu$sec and a heat flux of 5.1×10^8 W/m^2. This corresponds

to an 8 W laser focused into a 100 μm spot at 50 % reflectivity.

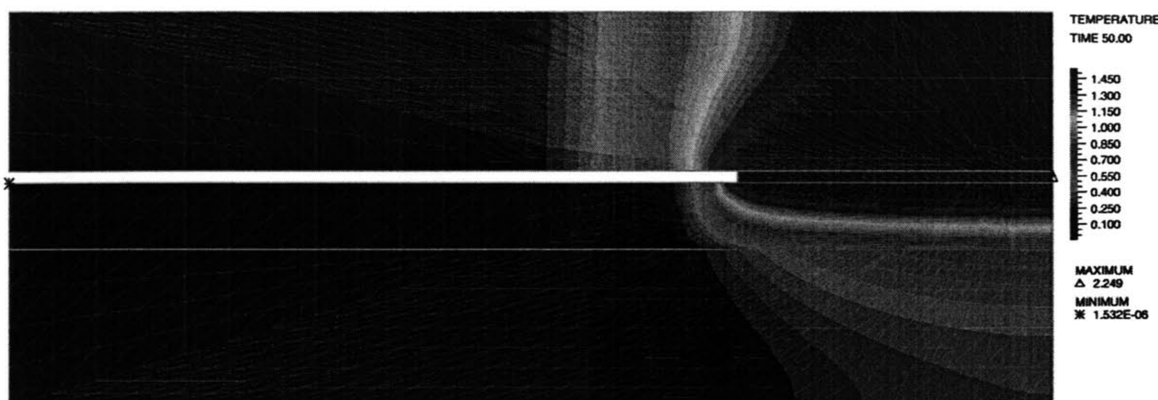

Figure 2-11: Temperature contour plot at t=15 μsec and a heat flux of 5.1×10^8 W/m^2

To gain more quantitative insight into the lateral temperature distribution, specific values are computed at the nodes along the top and bottom surfaces of the resist (lines A and B shown in Figure 2-10). The time evolution of the lateral temperature profile along the top and bottom surfaces is shown in Figure 2-12. In this particular case, the applied heat flux is $5.1{\times}10^8$ W/m^2. The solid curve depicts the profile at the end of the exposure, and the two dashed lines show subsequent temperature profiles after heating has stopped. Decreasing the thermal capacitance of the system by using thinner metal and thinner resist layers will reduce post-exposure heat diffusion.

The effects of the incoming energy flux on temperature distribution are shown in Figure 2-13. The lateral temperature profile along the top surface of the resist is shown for 3 different heat fluxes (5.1×10^8 W/m^2, 1.3×10^8 W/m^2, 5.7×10^7 W/m^2) that correspond to an 8 W laser at 50% transmittance focused into 100 μm, 200 μm, and 300 μm spots, respectively. Clearly, a higher flux produces sharper lateral temperature gradients. However, this benefit must be balanced with the accompanying larger temperature difference between the top and bottom resist surfaces. In order to cure the resist through its thickness the top surface must be substantially warmer than the bottom. Depending on the resist chemistry this may or may not cause problems at the top surface.

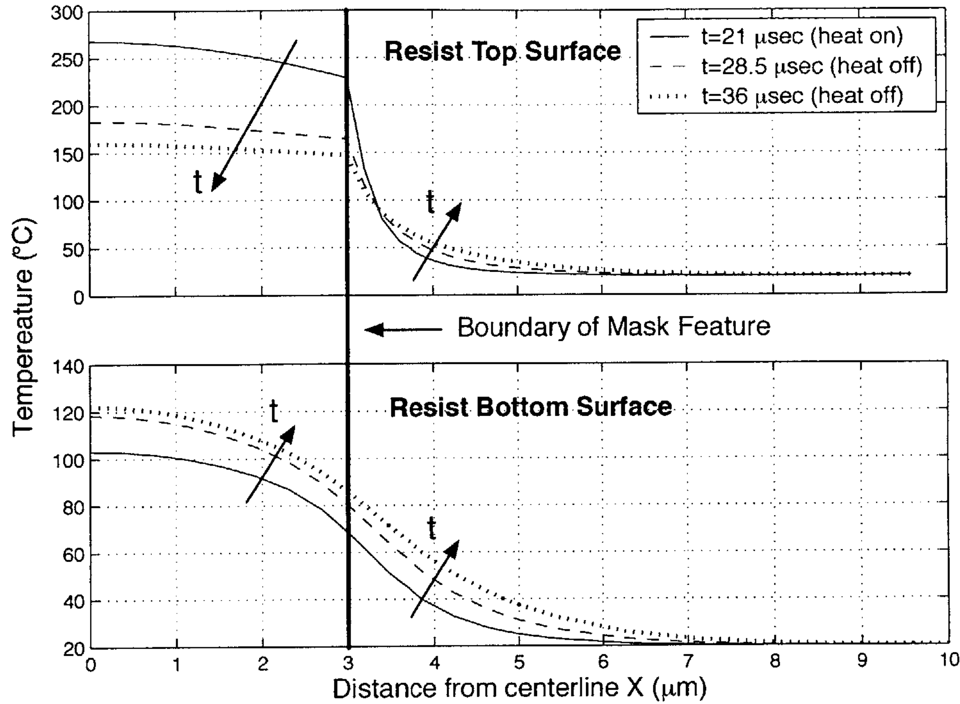

Figure 2-12: Time evolution of the lateral temperature profile along the top and bottom resist surfaces. At $t = 21$ μsec, heating is stopped and the temperature gradients soften. Along the top surface, the resist under the metal cools immediately while the resist adjacent to it increases in temperature. Along the bottom surface, temperatures increase everywhere as heat diffuses from the resist above.

The above results confirm that the primary means of increasing resolution is decreasing the thickness of the thermoresist layer. To illustrate this point, a simulation was performed using a mask feature 200 nm wide and a resist thickness of 20 nm. The model is shown in Figure 2-14. The metal layer was subjected to a heat flux of 5×10^9 W/m^2. A snapshot of the temperature profiles along the top and bottom resist surfaces at $t = 180$ nanoseconds is shown in Figure 2-15. As expected, the plot appears qualitatively the same as Figure 2-12 - the only difference is the higher heat flux and shorter time scale. In this case lateral thermal diffusion is roughly 25 nm.

There is a great deal of uncertainty in the preceding analysis. The primary source is the material characteristics, and in particular the properties of the thermoresist. Generic polymer properties were used in modeling, but as discussed in Section 2.3.1, specific examples may vary widely in their thermal conductivities and in their behavior

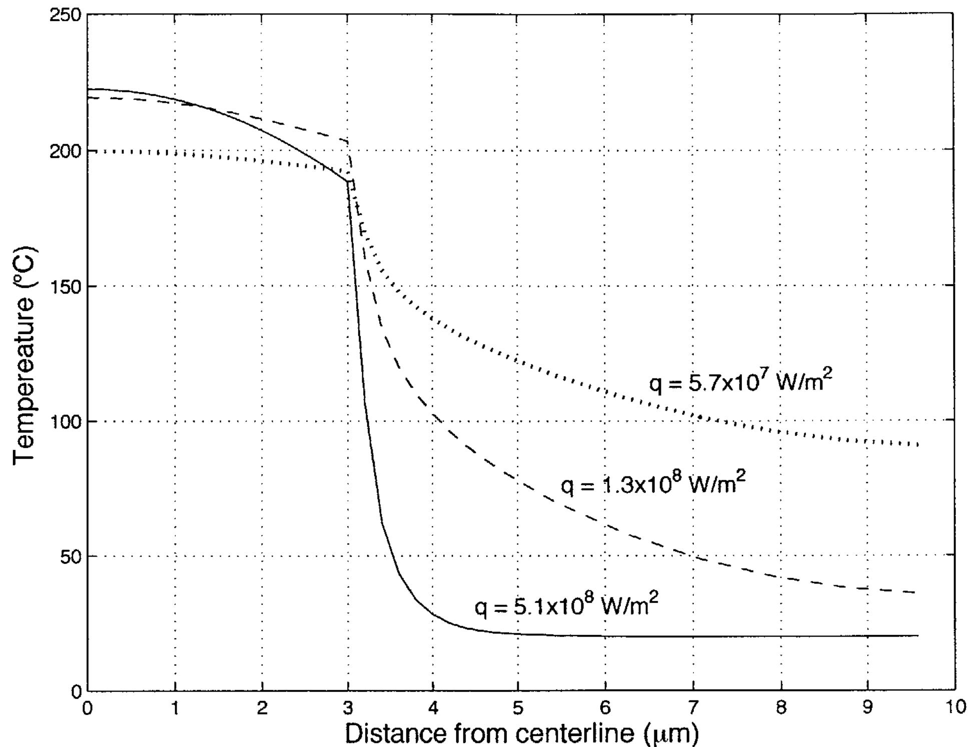

Figure 2-13: The lateral temperature profile along the resist top surface (line A) for 3 different heat fluxes. Higher flux produces sharper temperature gradients and potentially better resolution.

at high temperatures. Many of these polymers were developed for specific purposes and have not been studied in the wide range of conditions necessary to produce accurate data. The type of glass used as a mask substrate has an impact as well, since a pure crystal such as quartz will have a conductivity an order of magnitude higher than ordinary glass. Also, the effects of thermal contact resistance at the metal-resist interface and thermal expansion were not considered. These should be examined in future work.

The lateral temperature distribution alone is not sufficient to determine the lithographic resolution. The contrast of the thermoresist is also necessary. In the lateral direction temperature varies smoothly from a peak value down to zero, and the chemical properties of the resist determine where the crosslinking cutoff occurs and how sharp it is. Unfortunately such information is not often available, and this introduces still more uncertainty into the picture.

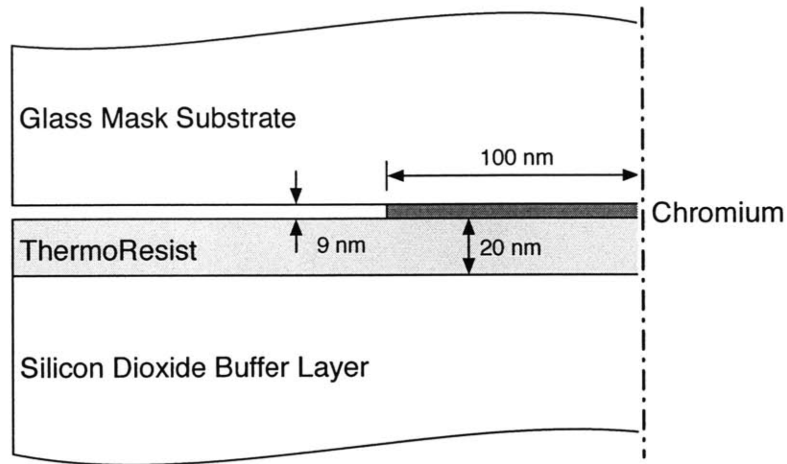

Figure 2-14: 2D model with reduced dimensions, illustrating the potential resolution of CTL.

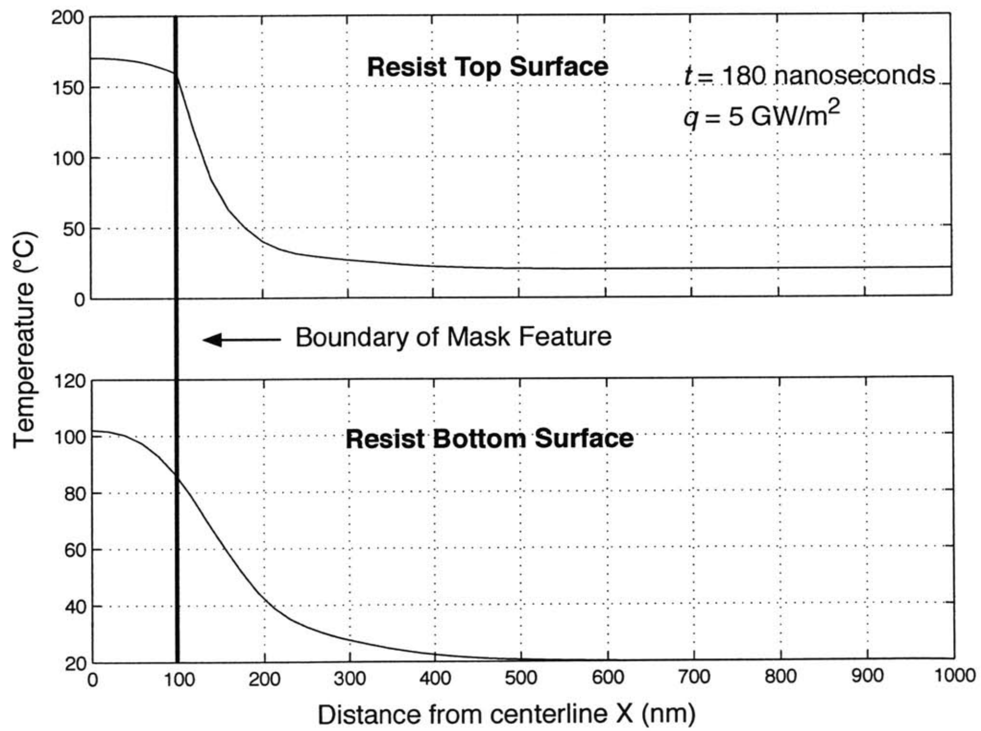

Figure 2-15: The lateral temperature profile along the top and bottom resist surfaces at t =180 nanoseconds. Lateral thermal diffusion is roughly 25 nm.

Despite these limitations, the thermal and optical models presented here have some value. They provide order-of-magnitude estimates on key values such as optical intensity and exposure time and give valuable qualitative insight into the effects of changing variables such as exposure flux and resist thickness. This information was put to use in constructing a basic CTL system, the details of which are discussed in the next chapter.

Chapter 3

Experimental Setup

A basic CTL system was built to demonstrate the feasibility of the method. Time constraints and a limited budget required that the system be made using easily obtainable parts and materials. The resulting apparatus and exposure method have very low throughput and are only capable of reproducing patterns on the order of a few microns. However, only a few basic changes would be necessary to increase both throughput and resolution.

The system can be broken into two main subsystems, an optics system and a wafer positioning system, plus a software scheme that ties the two together. The optics system includes a high power laser, a mechanism to create controlled short light pulses, lenses and mirrors. The pulse generator is a small scanning mirror which swings the beam through a wide arc. A thin slit positioned midway through the arc allows light through for a fraction of a second, and by varying the arc speed or slit width the pulse length can be controlled. The wafer positioning system consists of a vacuum wafer chuck to create intimate contact between the mask and wafer and a precisely controlled scanning stage to maneuver the wafer during exposure. Using custom software written in the LabVIEW environment, the two subsystems work together to characterize the incoming laser beam and to expose small regions of a silicon wafer coated with thermoresist.

An overview of the setup is shown in Figure 3-1. The details of the optics subsystem are described in the next section, followed by a description of the positioning

subsystem and LabVIEW control scheme. Finally, the choice of materials and mask design for the first tests is discussed.

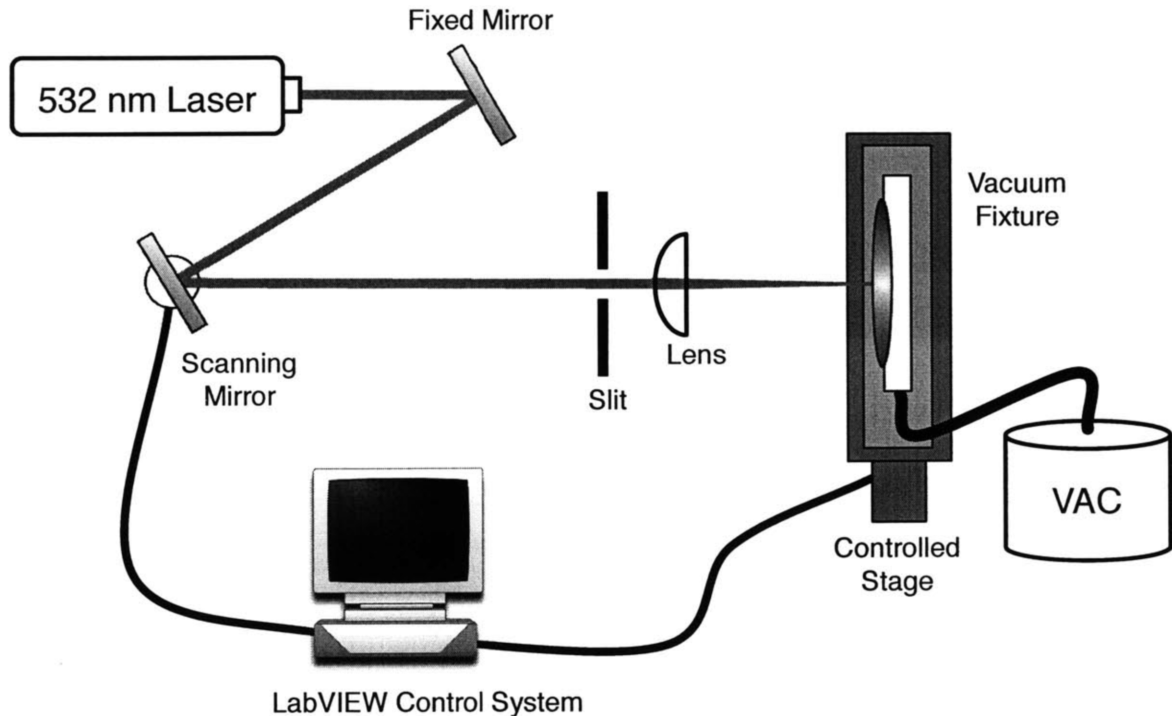

Figure 3-1: Schematic of the basic CTL system. A scanning mirror swings the beam past a small slit, generating a controlled light pulse. The wafer and mask are held together on a vacuum chuck which is positioned by a computer-controlled stage.

3.1 Optics

The exposure laser used was a Millennia VIIIs continuous wave laser produced by Spectra-Physics. It contains an Nd:YVO_4 doped crystalline matrix and can produce up to 8 W of power in a continuous wave at 532 nm. The beam is Gaussian in profile and roughly 2 mm in diameter at full width half maximum. This wavelength was suitable for several reasons. Glass (both soda-lime and fused silica) are non-absorbing at 532 nm, it does not cause crosslinking in most polymers, and in common metals such as Cr, Al and Fe the 95% absorption depth is less than 30 nm.

Based on the numerical models presented in Chapter 2, the laser should heat the

sample for a duration between 1 μsec and 100 μsec. The low end of this range is too fast for mechanical shutters, so a scanning mirror system was implemented instead. The basic arrangement in shown in Figure 3-2.

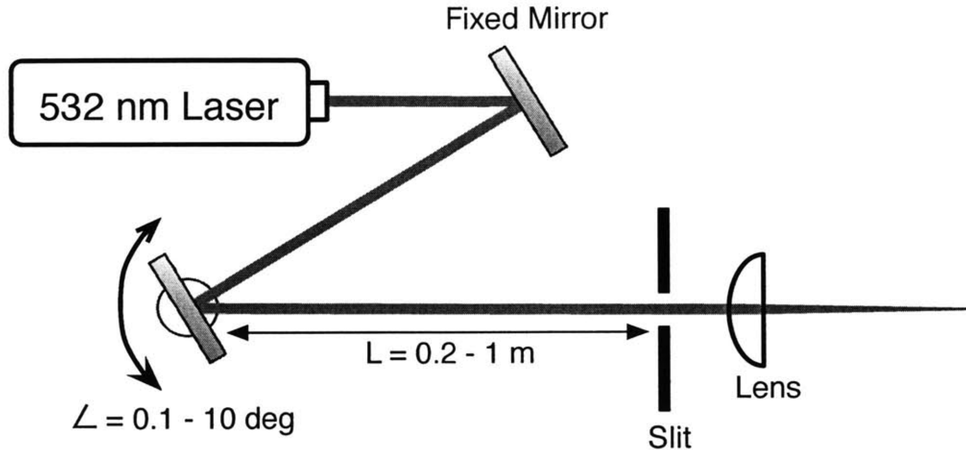

Figure 3-2: Pulse generation system consisting of a scanning mirror and slit.

The scanning mirror used was Optical Scanner Model 6210 from Cambridge Technologies, Inc. It consists of a 532 nm mirror mounted on a moving magnet motor. The mirror is capable of steering a 3 mm beam. The motor can produce large amounts of torque very quickly and thus has fast step response, on the order of 100 μsec. An input signal is sent to the scanner's controller and the mirror responds by tracking the signal.

Two factors influence the pulse duration - the distance L between the mirror and the slit, and the angular speed of the mirror. In this setup, the distance L was used for gross control and the angular speed was used for fine control. The slit width was kept constant at 3 mm to allow the full beam through. A step input was sent to the scanner via the computer. The mirror swung from one end of its range to the other and the laser passed the slit midway between the two extremes. By controlling the size of the step impulse (and through that the angular excursion of the mirror), the peak speed can be adjusted for fine control. Figure 3-3 shows the relationship between angular excursion vs. pulse width for a distance $L = 0.9$ m. The pulse width at each input level was measured using a fast photodiode connected to an oscilloscope.

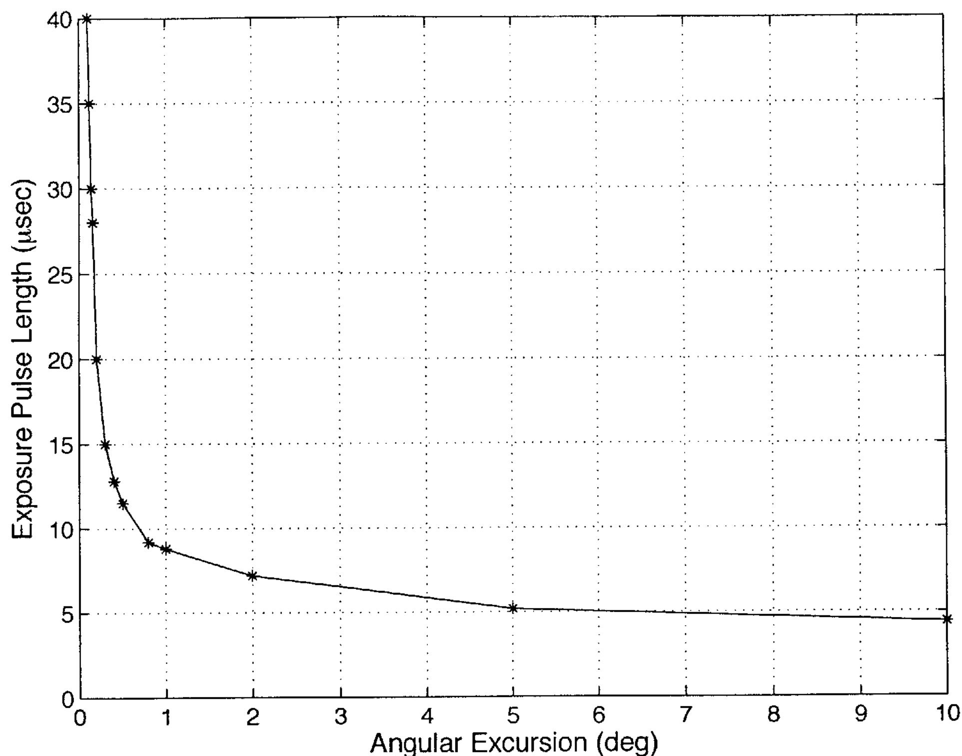

Figure 3-3: Pulse length as a function of angular step size as measured by a photodiode. The distance between the mirror and the slit is $L = 0.9$ m.

After the laser pulse passes through the slit, it is focused by a lens with a focal length of 5 cm. In order to determine the intensity at the mask surface, the focused beam diameter must be known. The beam was characterized by the simple method of slicing into the beam with a razor blade and recording the integrated intensity as a function of position. Differentiating this data produces a plot of the beam's intensity profile. A diagram of this scheme is shown in Figure 3-4.

The lens was mounted on a micro-positioning stage so that it could be moved parallel to the beam. By measuring the beam profile at several Z positions, the correct lens position for a desired spot size (and therefore intensity) could be determined. Figure 3-5 shows a typical beam profile that was captured. The smallest attainable profile with this lens/laser combination was around 10 μm at full width half maximum.

The depth of field of the lens was found by recording the spot size at several Z locations. This makes it possible to translate estimated errors in lens positioning

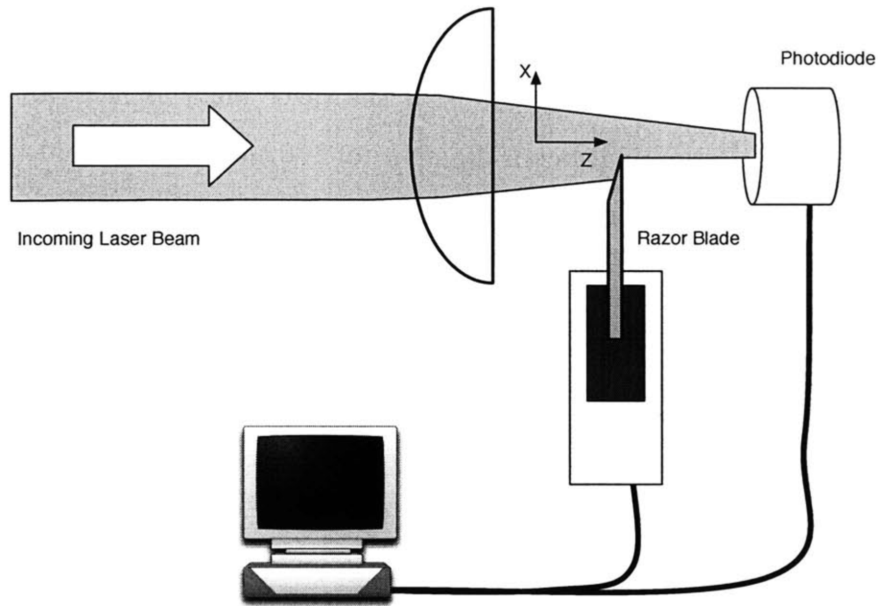

Figure 3-4: Beam profiling technique used to characterize the laser intensity at the mask surface. A computer records the integrated intensity at different positions and differentiates the results.

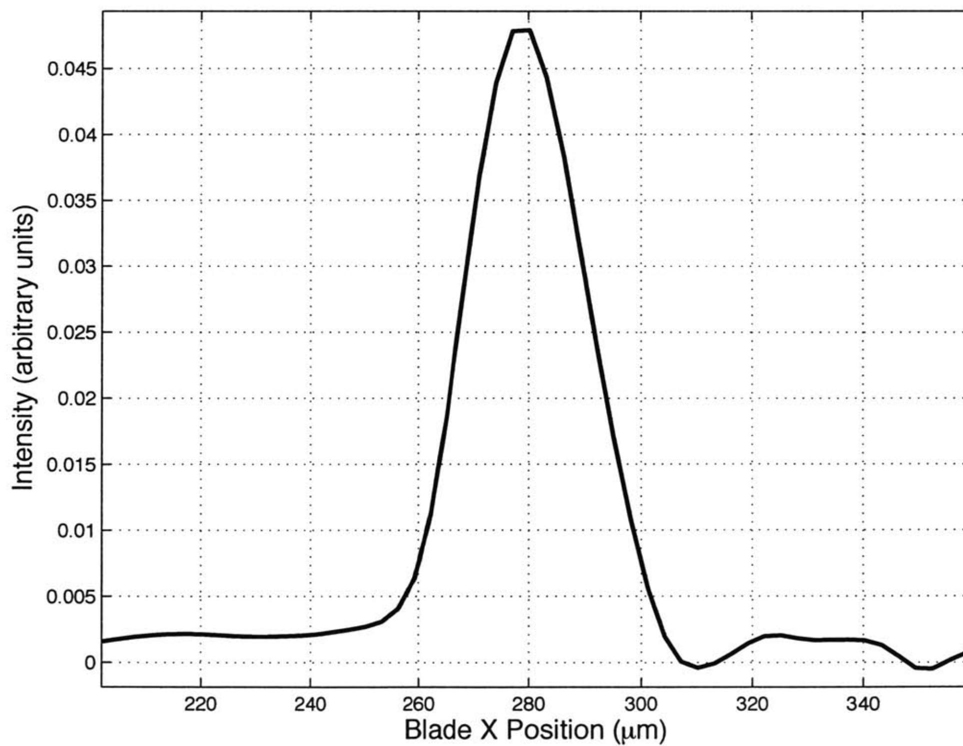

Figure 3-5: A typical beam profile captured using the beam slicing method.

accuracy into errors in optical intensity. With the current system, the ability to place the wafer surface at the same plane as the razor blade is accurate to within roughly 500 μm. For a nominal beam diameter of 100 μm, a positional uncertainty of $Z = \pm 500\mu$m gives an uncertainty in optical intensity of $\pm 40\%$.

3.2 Wafer Stage

The biggest mechanical challenge in implementing a CTL system is to maintain good thermal contact between the mask and the wafer over large areas. Fortunately, a number of solutions to the problem have been developed for use in other situations. The approach described here was developed for use in contact optical lithography and employs a thin, flexible mask that deforms to match the wafer surface. The general approach and mechanical designs were suggested by Dr. James Goodberlet.[16]

Figure 3-6 shows the vacuum fixture used to maintain intimate mask-wafer contact. The basic design is simple. Two thin metal plates, approximately 6"×6", sit on a 0.25" thick sheet of natural rubber. A standard 4" wafer and photomask are placed inside a square window cut in the two plates. On the bottom plate, a thin groove has been cut along the inside edge of the square window. The groove connects to a vacuum port and allows the air between the mask and wafer to be drawn out evenly from all sides. A close view of the bottom plate groove is shown in Figure 3-7. A rubber top layer covers the mask and wafer, sealing the top surface. The final arrangement is shown in Figure 3-8.

With the top seal in place, a small roughing pump was connected to the vacuum port. Good mask-wafer contact is easily verified by inspection. Figure 3-9 is a photograph of a mask and wafer under vacuum. Any dust particles are surrounded by colorful interference patterns commonly referred to as Newton's Rings. These are visible under ordinary white light, but are often more dramatic when viewed with a monochromatic source. The dark patches between the rings are regions of good contact.

The vacuum fixture assembly was mounted on a computer-controlled motion stage,

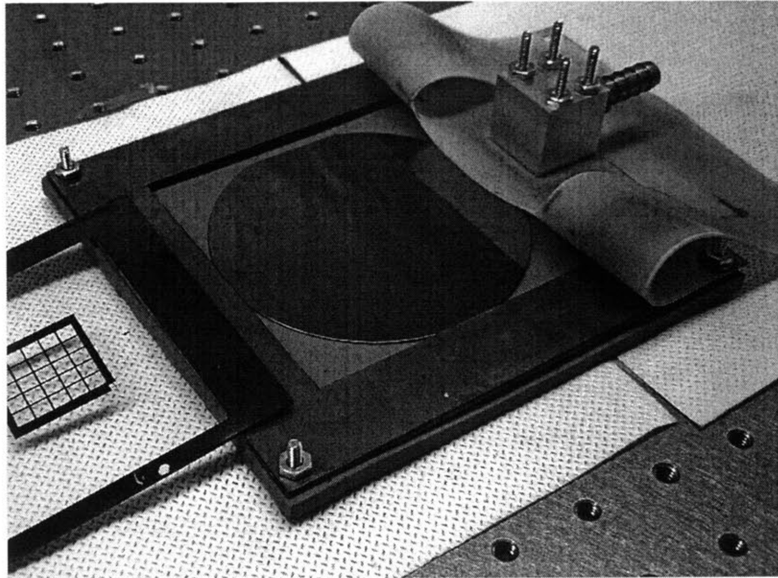

Figure 3-6: Vacuum wafer fixture used to maintain intimate mask-wafer contact

Figure 3-7: A close view of the groove cut on the bottom plate. The groove allows air to be drawn out from between the mask and wafer.

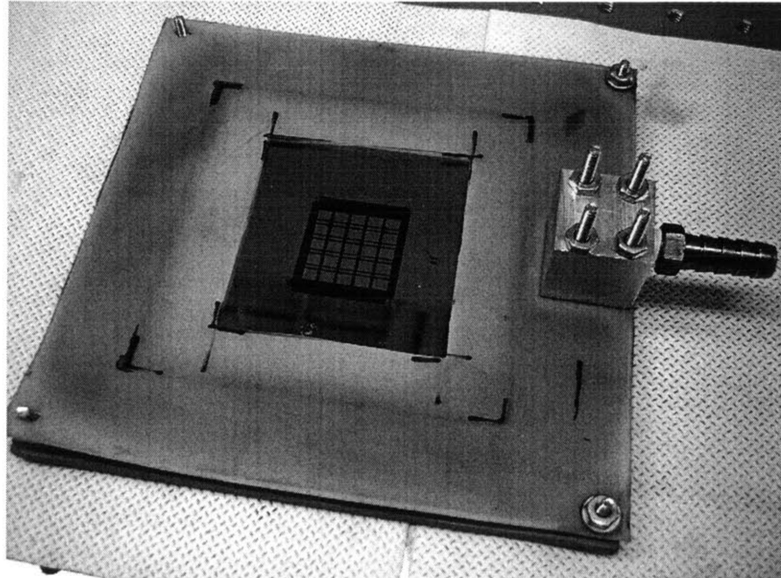

Figure 3-8: Vacuum wafer with top seal in place.

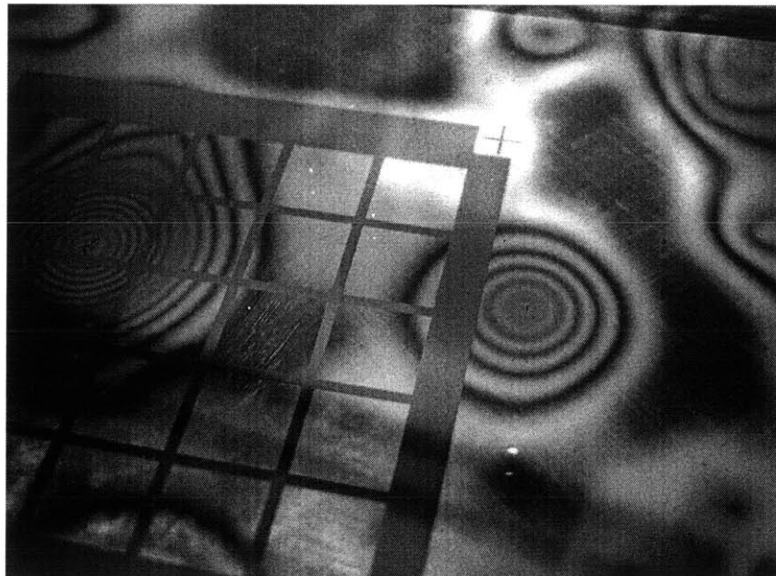

Figure 3-9: Newton's rings between the mask and wafer under vacuum. On this dirty sample it is easy to see dust particles and dark regions of good contact.

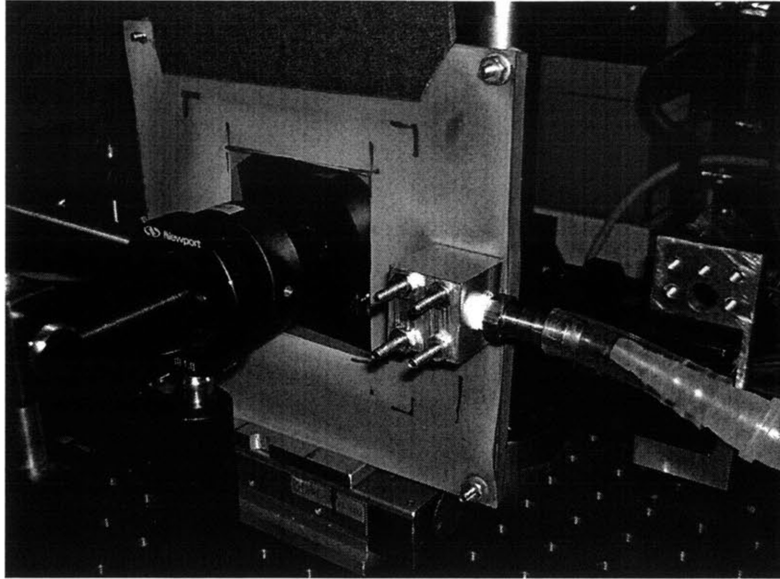

Figure 3-10: Vacuum wafer assembly mounted on a motion stage. The stage was controlled by a LabVIEW program and moved in 0.1 μm increments.

as shown in Figure 3-10. The stage used was a Klinger CC1 and had a nominal step size of 0.1 μm. Motion of the stage was controlled using LabVIEW software. The software synchronized the stage motion with the operation of the scanning mirror, enabling exposure of areas larger than the laser spot size.

3.3 Materials Selection

The most critical material for the CTL process is the thermoresist polymer. The type of polymer used determines the crosslinking temperature, resolution, edge sharpness and the resist layer thickness. Unfortunately, not many polymers have been studied with the purpose of local crosslinking in mind. For the vast majority of polymers, little data exists on thermal resolution or thermal contrast. In addition, as discussed in Section 2.3.1 bulk material properties such as thermal conductivity and heat capacity may change in very thin film configurations. Thus, choosing a polymer that is well suited to thermal lithography is challenging.

In order to avoid the difficulties of finding, testing and characterizing suitable resist polymers, an off-the-shelf solution was selected for initial testing. The polymer

chosen was a commercially available photoresist, AZ 5214-E (Clariant Corp), that has been optimized for image reversal. In normal image reversal lithography, selected portions of the wafer are exposed with UV light, generating an acid in the resist layer. The wafer is then heated in an oven, and the areas that contain acid crosslink and become insoluble. In CTL, the inverse of this approach is used: the wafer is flood-exposed with UV light, generating acid everywhere in the resist. Then, when the metal mask features are brought into contact and heated, local crosslinking occurs.

Using AZ 5214-E has several benefits. As a common optical resist, it is relatively well studied. The optical properties and crosslinking characteristics are known: it is transparent at 532 nm, and after exposure to UV light will crosslink at roughly 110 °C. It is approved for use in most clean rooms, and can be developed with standard chemicals. Unfortunately detailed material property data is not available, so typical polymer properties are assumed. A more thorough investigation of the resist's properties should be undertaken in the future. The details of the process flow using this resist are presented in the next chapter.

The selection of the pattern mask is a much simpler job. The requirements are that the mask substrate be thin and optically transparent at 532 nm, and that the metal layer be strongly absorbing. A standard 4" chromium on glass mask meets these requirements. The substrate chosen for the first test masks was 0.020" soda lime glass, inexpensive and easily available. The masks were patterned with 90 nm of Cr in test patterns consisted of 8 μm gratings. Two variants were tried: an even pitch, with 8 μm Cr stripes and 8 μm spaces, and an every-other pitch, with 8 μm Cr stripes and 16 μm spaces.

A standard 4" silicon wafer coated with 1.2 μm of SiO_2 was used as a substrate. The wafers were coated with AZ 5214-E and exposed at a variety of power levels. The detailed procedure and some results are presented next.

Chapter 4

Method and Results

4.1 The CTL Process Flow

The CTL process was carried out in three stages. The first involves wafer preparation and coating. These steps were done in MIT's Exploratory Materials Laboratory (EML), a class 1000 fabrication space. Next is the exposure stage, which consists of mounting the wafer and mask in the fixture described previously and illuminating various regions with the 532 nm laser. This took place in the Rohsenow Heat and Mass Transfer Laboratory, where the CTL apparatus had been constructed. The final steps were development and etching, and these were done in EML.

Substrate preparation is straightforward. The wafers are subjected to the following processes:

1. Dehydration bake at 150 °C, 30 minutes
2. Spin coat with adhesion coating HMDS (Hexamethyldisilazane)
3. Spin coat with dilute AZ 5214-E, 4500 RPM, 40 seconds
4. Soft bake at 90 °C, 30 minutes
5. Flood exposure, $\lambda = 365$ - 436 nm, Energy > 100 mJ/cm^2

While waiting for step 1 (dehydration bake) to complete, the resist was prepared. The standard AZ 5214-E was diluted with PGMEA (propylene glycol methyl ether

acetate) to a mixture of 2 parts resist to 1 part solvent. This allowed for a thinner coat than the manufacturer's 1.4 μm specification. A profilometer was used to ascertain the resist film's thickness, approximately 450 nm.

After flood exposure, the wafer and mask were blown clean with nitrogen and the mask was placed Cr side down onto the resist surface. Two pieces of adhesive tape were used to hold the mask and wafer in this configuration. This prevented dust from contaminating the interface during exposure in the Rohsenow lab, which is not a clean environment.

The exposure process was carried out using software written in LabVIEW. The sample was placed under vacuum contact and put on the motion stage. The power level of the laser was set at the desired value, and the exposure program started.

The regions exposed were typically single lines, roughly 100 μm in width and several millimeters in length. These regions were easily found with an optical microscope and took around one or two minutes to expose. The exposure process itself was simple. The laser was left on continuously, and the software would use the scanning mirror to swing the beam past the slit, exposing a 100 μm spot for the desired amount of time, usually 30 μsec. Then, the program would shift the stage over by a set amount, normally some significant fraction of the beam diameter, and expose again. This process was repeated for the desired number of steps, usually about 50. An image of the LabVIEW software and a more detailed description of its function are included in Appendix B.

The post-exposure process consists only of developing the resist. The was done by immersion in AZ 422 MIF developer for 90 seconds with mild agitation. The result is a replication of the mask features in cured resist. Thus, CTL is a positive lithography process. The remaining resist features can be used as an etch mask for subsequent processing.

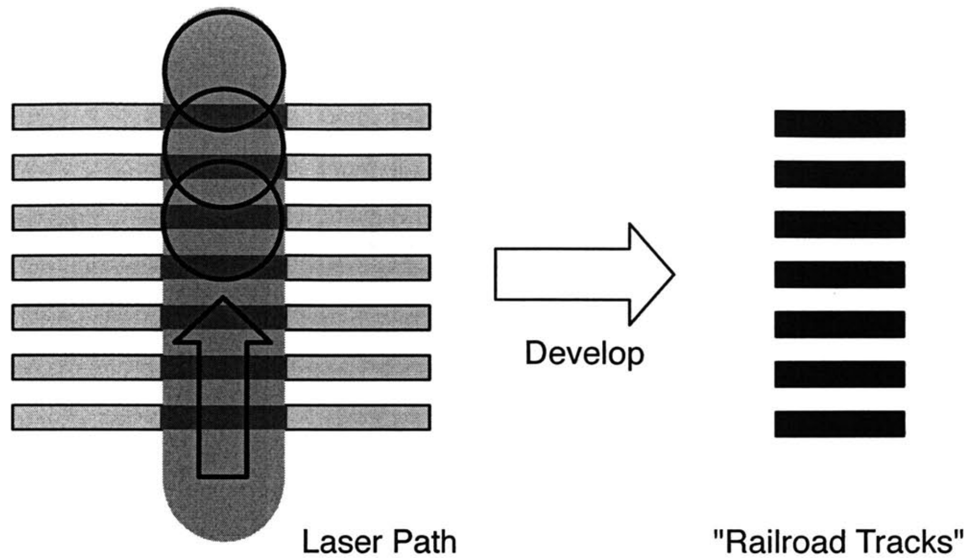

Figure 4-1: The exposure procedure and expected results. As the beam is stepped across the wafer it heats the metal stripes and leaves a "railroad tracks" pattern of cured the resist.

4.2 Results

The results presented now were produced using a 100 μm spot size and an exposure time of 30 μsec. The step size between spots was 70 μm, giving a good degree of overlap. The laser power level varies between 4 W and 8 W.

Figure 4-1 is helpful in interpreting the images that follow. It illustrates the exposure process and shows how a perfect set of results would appear. As the laser spot is moved across the grating in increments, the heated metal cures the resist below, leaving behind a "railroad tracks" pattern. The width of the tracks is determined by the diameter at which the beam intensity falls below some critical intensity threshold.

A representative sample of early results is shown in Figure 4-2. The images were obtained using an optical microscope at 20×, 40× and 60× magnification, respectively. The dark features are regions of cured resist that remained after the wafer was put through the development process. The pattern of tracks is clearly visible, with a pitch of 8 μm.

Although some semblance of the mask features was transferred to the resist, the results are far from being an accurate reproduction. The individual tracks are not

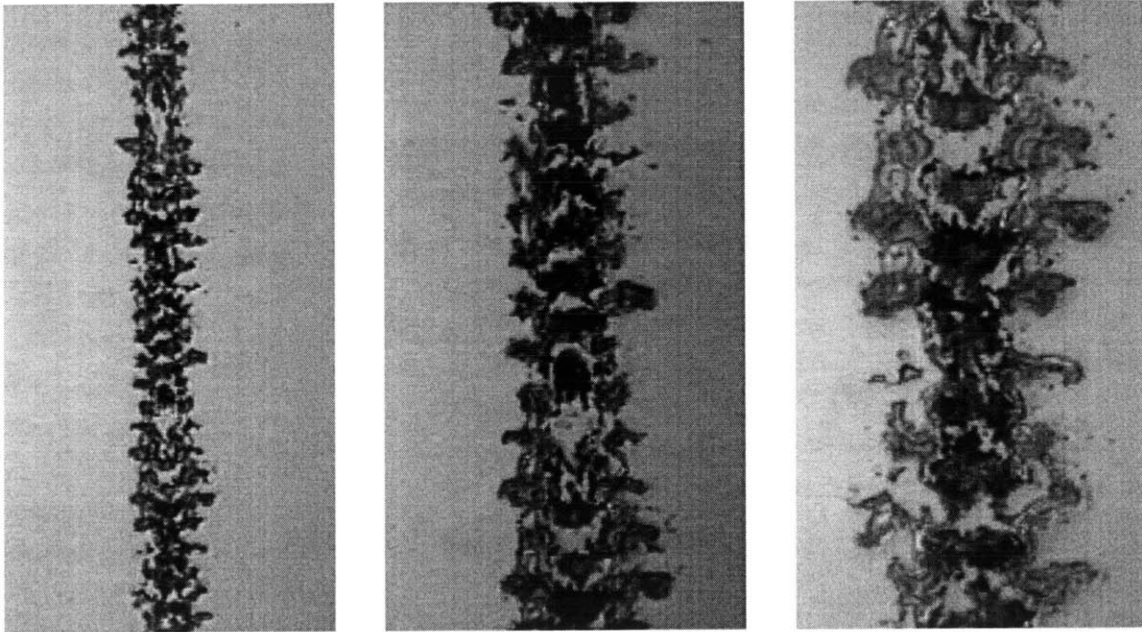

Figure 4-2: Early test results, showing cured resist features at an 8 μm pitch.

clean and rectangular, the spaces between the tracks are not free of cured resist, and large regions of the pattern appear to be torn away.

The primary cause of these defects is adhesion between the metal features and the resist layer. Figure 4-3 shows some samples that highlight the problem. In these cases, it is easy to see where large chunks of resist have been torn away during the separation process. This is consistent with observation that the mask and wafer must be pried apart following the exposure process. Examination of the mask after separation shows the problem even more clearly. Some post-exposure masks are shown in Figure 4-4. In this figure, the light stripes are the Cr features. The majority of the resist appears stuck to the Cr, with very little resist stuck to the glass regions between the stripes.

Unfortunately, the gross nature of the defects produced by adhesion makes it difficult to observe other aspects of interest in the results. The degree of lateral heat diffusion and the properties of the resist sidewalls are obscured, along with the effects of modest variations in applied power levels. However, there is still valuable information to be gained from these images.

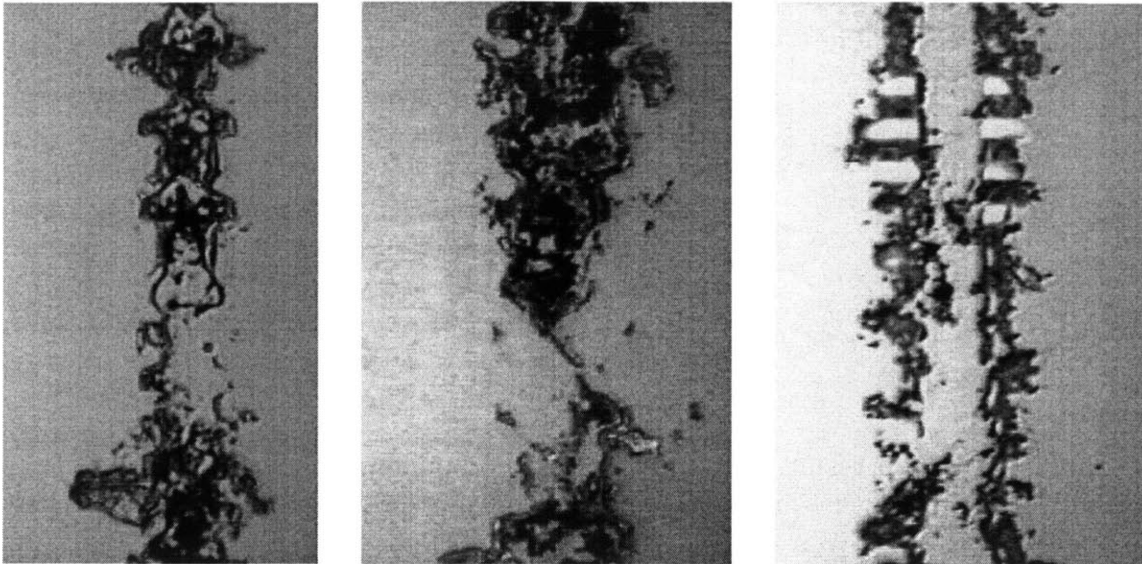

Figure 4-3: Regions on the mask where resist has been torn away by adhesion.

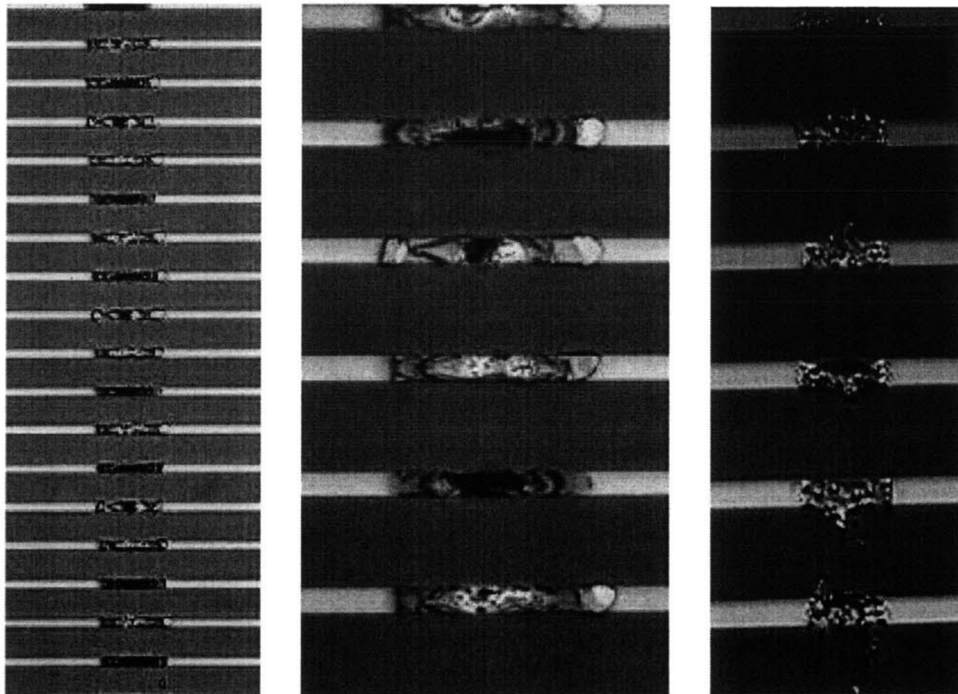

Figure 4-4: Images of the photomasks following laser exposure.The light stripes are Cr features. Most of the cured resist has stuck to the Cr and has been torn from the wafer, while very little resist appears on the glass areas.

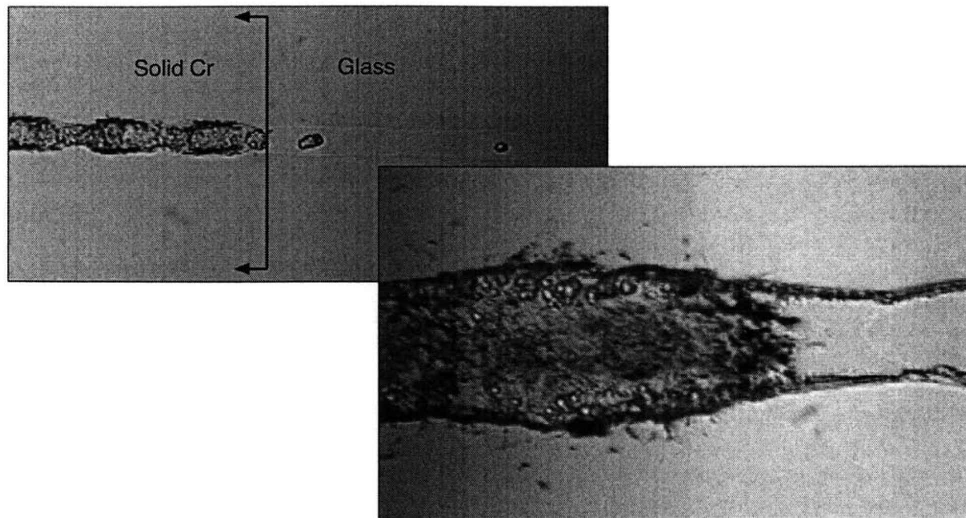

Figure 4-5: Pattern resulting from exposing the boundary between a region of solid Cr and clear glass, using an 8 W beam at a 100 μm spot size. It is clear that the Cr is being heated selectively and curing the resist below, although at this power level the resist is slightly affected by the laser alone.

The vacuum fixture is successful in creating intimate contact between the mask and wafer, and the contact is adequate to transfer enough energy to cure the AZ 5214-E. Also, it is clear that regions in contact with Cr features are being cured while surrounding regions are not. This indicates that, as expected, the glass and resist are largely transparent and that the Cr is absorbing a substantial fraction of the incident energy. To test the selective heating more explicitly, a portion of the mask consisting of the boundary between a large uninterrupted region of Cr and clear glass was exposed. The result is shown in Figure 4-5.

The portion of cured resist on the left was in contact with solid Cr while the right half had only glass above it. This sample was exposed at the highest power level, 8 W. At this power the individual spots are visible, indicating that perhaps a smaller step size between spots should be used. Also, at this high power level the laser appears to have a slight effect on the resist itself - while the left half of the images are clearly more developed, a faint outline of the beam path is visible in the right half.

Solutions to the adhesion problem and the future of contact thermal lithography are discussed in the final chapter.

Chapter 5

Discussion and Conclusion

5.1 Short Term Goals

The most immediate challenge for contact thermal lithography is to overcome the strong adhesion between the mask features and the resist. The adhesion destroys most of the detail in the transferred pattern and makes it impossible to analyze the finer aspects of the process. Fortunately, there are a number of potential solutions to the problem, some of which are currently being tested.

The most obvious solution is to apply an anti-adhesion coating to the mask surface. Qualities that the coating must have include a low surface energy, good durability (100's or 1000's of cycles), thermal stability up to at least 200 °C, and minimal thermal resistance. Fortunately there is a wide variety of coatings available.

One of the most promising classes of coatings is self-assembled monolayers (SAMs). SAMs are formed when chemical precursors react at the substrate surface to form interlocking molecular networks. A variety of SAMs have been used as anti-adhesion coatings with great success. Most are characterized by a silane group and have low surface energy. The more common ones include OTS (octadecyltrichlosilane), DDMS (dichlorodimethylsilane) and FDTS (1H, 1H, 2H, 2H-perfluorodecyltrichlorosilane).[17, 18, 19] These coatings vary in their stability and ease of application, but all have the potential to meet the requirements of CTL.

Thus far, only one anti-adhesion coating has been attempted for CTL. The SAM

used was (tridecafluoro-1,1,2,2,tetrahydrooctyl trichlorosilane), a product from Gelest, Inc. This coating has been successfully used as a release agent for Step-and Flash Imprint Lithography, where it was found to be extremely durable and had a surface energy around 12×10^{-3} N/m.[20]

The coating was applied in the vapor phase following the procedure described for SFIL by Bailey et. al.[20] Unfortunately, for the particular combination of mask metal and resist that was being used in the current situation, the coating actually created a stronger bond between the mask and wafer. At the elevated exposure temperatures, the SAM coating allowed the Cr to react with the AZ 5214-E and form a bond sufficiently strong to tear the Cr from the glass substrate during separation.

Despite this setback, the adhesion problem appears tractable. The other SAMs mentioned above may eliminate the problem. Also, it is possible that switching the mask metal from chromium to aluminum or iron will allow the Gelest coating or one of the other SAMs to work. Currently, tests are underway involving both Cr and Al masks and a number of surface coatings.

After adhesion has been eliminated, two critical tasks are to more carefully characterize the thermal behavior of the system and to explore alternative thermoresists. Without the gross tearing that results from adhesion, fine features such as edge resolution should be discernable. Examination of resist edges will give insight into the lateral heat diffusion and the effects of varying the optical intensity and duration. The edge detail will yield information about the performance of AZ 5214-E as a thermoresist as well. Although it served well as a quick means of testing CTL, AZ 5214-E was developed and optimized for a different purpose. There are numerous polymers that crosslink in the neighborhood of of 100 - 200 °C and it is possible that one of these is better suited as a thermoresist. Alternative polymers should be evaluated and tested.

5.2 Long Term Goals and Commercial Potential

The long term goals for CTL are to push resolution to its lower limits, and to take the technology from a laboratory experiment to a viable fabrication process.

The ultimate resolution of CTL appears to be limited by the thermoresist layer. The transient thermal analysis presented in Chapter 2 shows that lateral thermal diffusion will result in temperature contours that extend out from the edges of mask features by roughly the thickness of the resist. Although material anisotropy may alter this behavior somewhat, the thickness will still be the dominant resolution limiter.

Therefore, reducing the resolution of CTL is primarily an issue of reducing the resist thickness. This will present a number of materials challenges. It is possible to apply very thin polymer coatings to wafers. For example, PMMA can be spun on to thicknesses of less than 50 Å.[21] However, finding a thermoresist that will reliably crosslink at such thicknesses may be difficult. In addition, in order to reliably serve as an etch mask at such thicknesses, the resist must be etched with a highly selective process. Reducing the resist thickness and developing an accompanying etching process will likely be the main challenge in extending the resolution of CTL.

A more straightforward issue is switching the light source from a narrow laser beam to a more powerful system that can achieve similar intensities over much larger areas. This would improve exposure times to acceptable levels. For example, if the spot size were one centimeter and it took one second to step from one location to the next, a 4" wafer could be exposed in around 90 seconds.

Additional challenges facing CTL are common to other alternative lithography techniques. These include issues with multi-level alignment and planarization. Fortunately, numerous groups are aware of these problems and are actively developing a variety of solutions. To take one example, alignment techniques developed for SFIL have reduced multilevel placement errors to 500 nm.[22] The first commercial CTL machines could be constructed by retrofitting existing equipment that had been designed for a different type of lithography. A contact photolithography machine, for example, could be very similar mechanically and require only the addition of an

appropriate high intensity light source.

5.3 Conclusion

Contact thermal lithography is a new approach to pattern reproduction. It shares similarities with other contact lithography techniques such as optical contact lithography, nano imprint lithography and step-and-flash imprint lithography. However, it is distinct from these approaches in that it uses optical to thermal energy conversion in the pattern mask and thermal conduction from the mask to the resist layer to transfer the pattern. This gives CTL a number of attractive features, such as the ability to replicate truly arbitrary patterns, a contact pressure requirement of only 1 atm, and a resolution limited primarily by the thickness of the resist layer.

The basic concepts of the CTL system were presented in this thesis. The general geometry and process flow were covered in the first chapter. An analysis of some essential elements of the process, such as the optical characteristics of the mask and the transient thermal behavior, were presented next. This included basic order of magnitude estimates as well as more detailed finite element modeling. An overview of the first CTL system, a simple proof-of-concept apparatus, was given, and some of the first results presented.

The essential features of CTL, namely optical to thermal conversion in the mask layer and pattern transfer from the mask to the wafer, were successfully demonstrated. However, the results were marred by adhesion between the mask and resist layers. This presents the most immediate challenge to CTL, but can likely be overcome through the use of an appropriate mask surface treatment. Other important work includes exploring alternative resist chemistries and characterizing the exposure process more thoroughly. Finally, long range goals for CTL include increasing resolution by reducing layer thickness to below 100 nm, and developing CTL machines suitable for commercial production.

Appendix A

Material Properties

A.1 Optical Properties

Optical properties for the materials used in modeling were taken from *Handbook of Optical Constants of Solids III* by Edward Palik.[23] The refractive index $\overline{N} = N - ik$ is given over a wide range of wavelengths. A portion of this data for the relevant materials is presented graphically below.

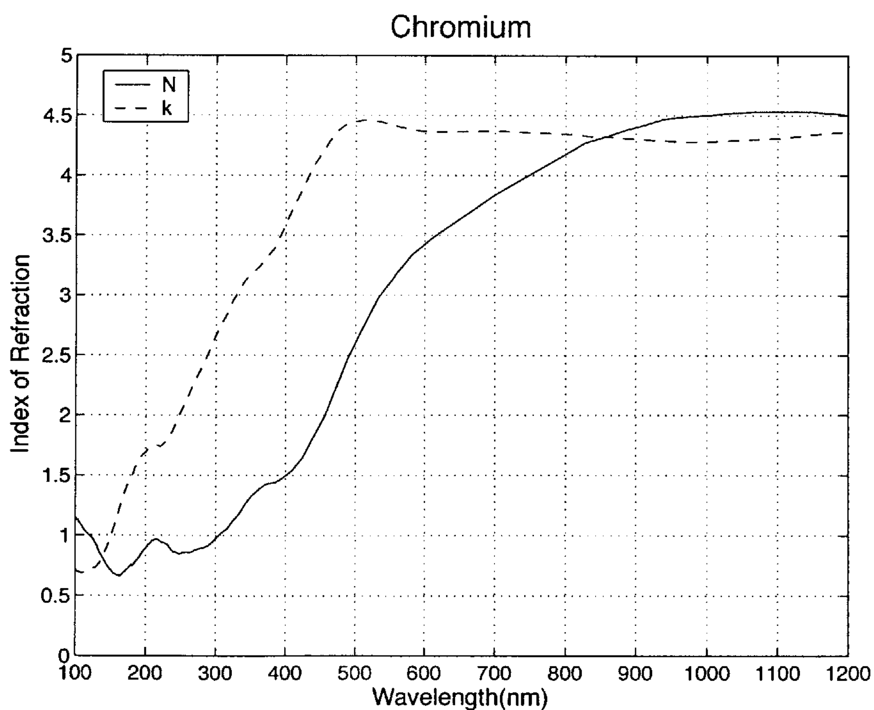

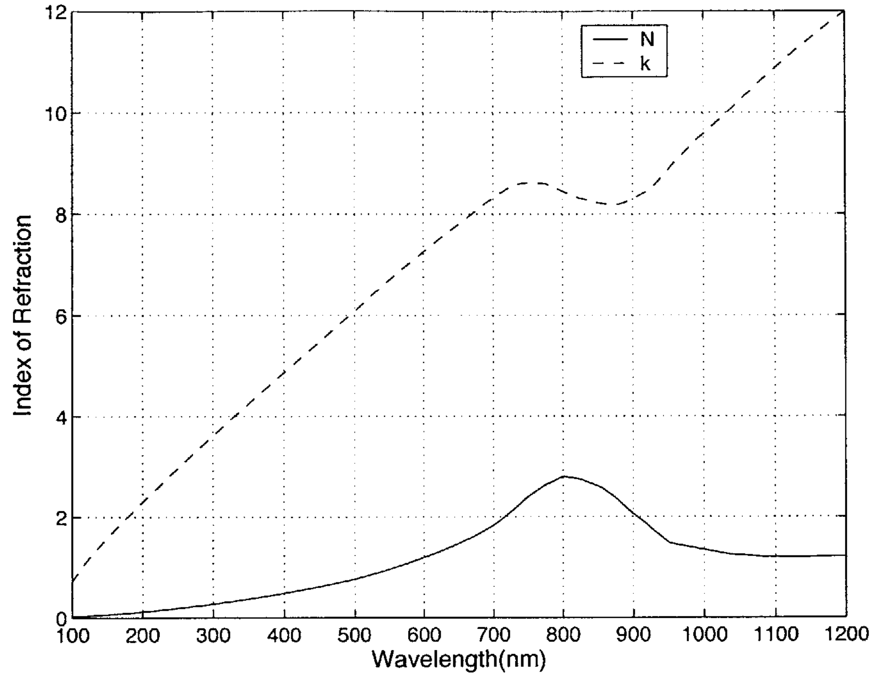
Aluminum
N
k
Index of Refraction
Wavelength(nm)
0
2
4
6
8
10
12
100
200
300
400
500
600
700
800
900
1000
1100
1200

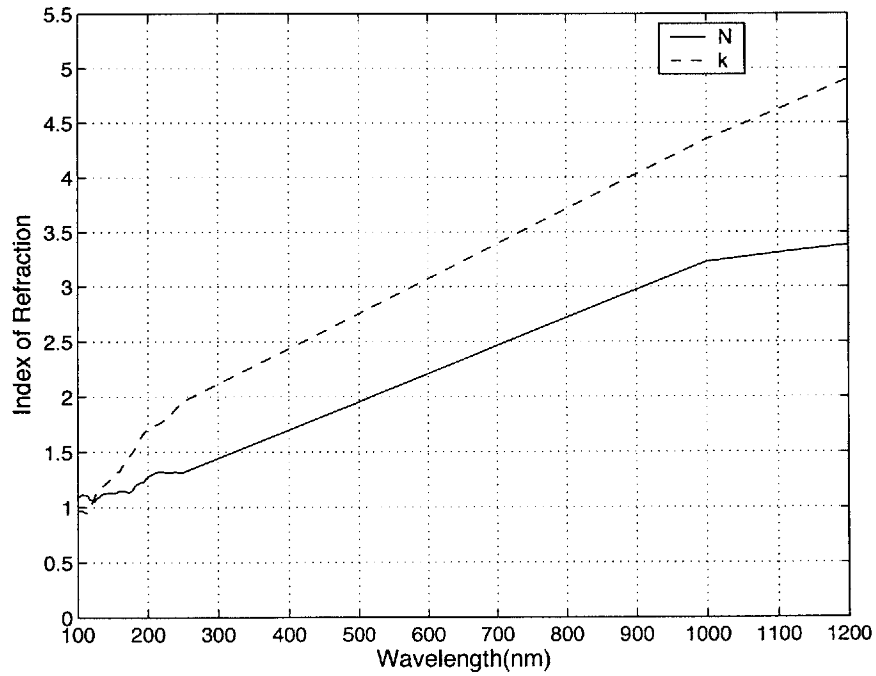
Iron
N
k
Index of Refraction
Wavelength(nm)
0
0.5
1
1.5
2
2.5
3
3.5
4
4.5
5
5.5
100
200
300
400
500
600
700
800
900
1000
1100
1200

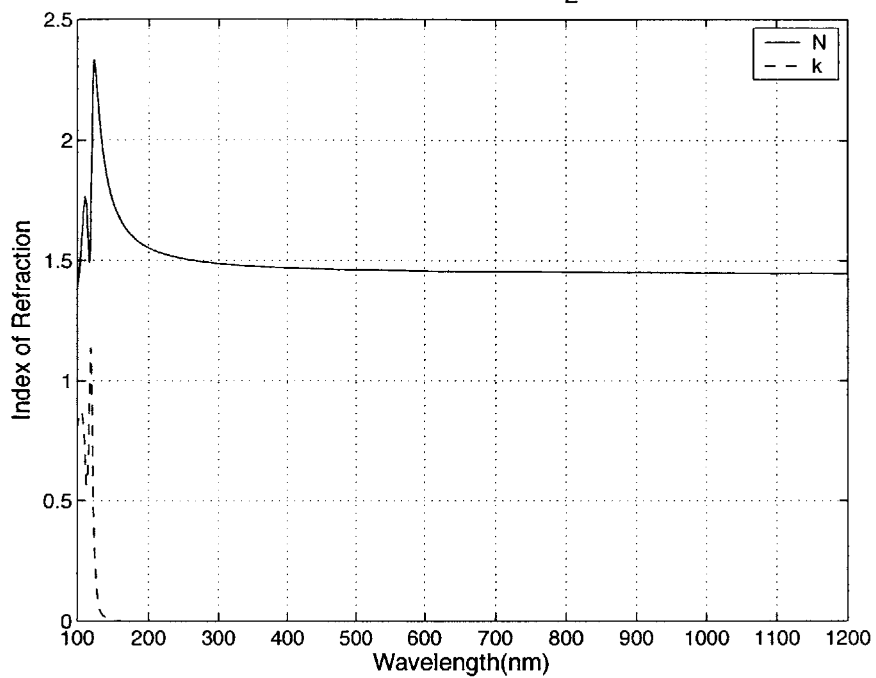

Amorphous SiO_2
Index of Refraction
Wavelength(nm)
N
k
0
0.5
1
1.5
2
2.5
100
200
300
400
500
600
700
800
900
1000
1100
1200

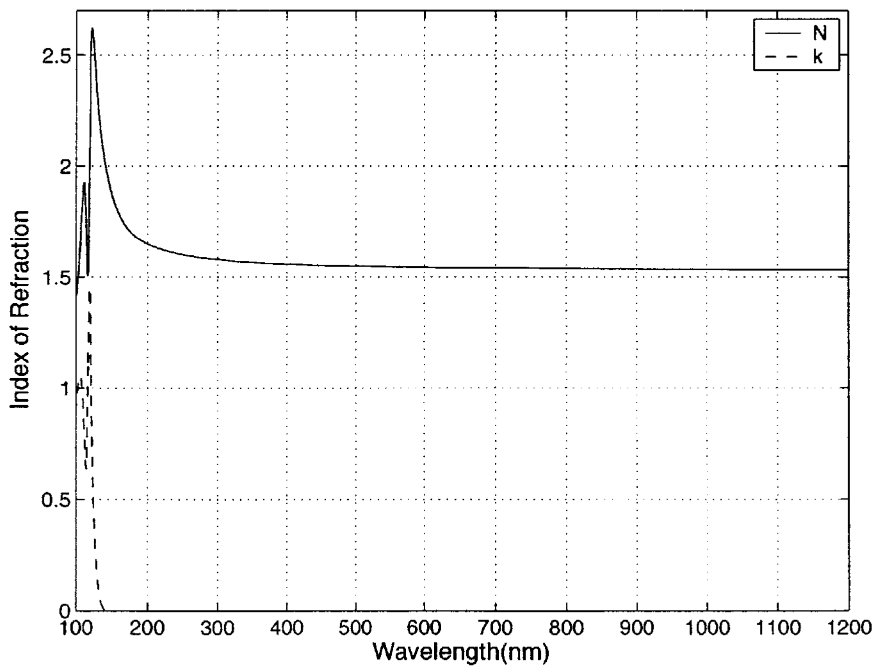

Quartz
Index of Refraction
Wavelength(nm)
N
k
0
0.5
1
1.5
2
2.5
100
200
300
400
500
600
700
800
900
1000
1100
1200

A.2 Thermal Properties

Unless otherwise noted, thermal material properties were taken from *A Heat Transfer Textbook* by Lienhard and Lienhard.[15] Data are given for $T = 20$ °C.

Table A.1: **Thermal Properties**

Material	ρ (kg/m^3)	c_p (J/kg·K)	k (W/m·K)
Chromium	7,190	453	90
Aluminum	2,707	905	237
Iron	7,897	447	80
PMMA[24]	1,170	1,466	0.17
Fused Silica	2,200	745	1.38
Quartz, $\perp$ to c-axis	2,640	743	6.21

Appendix B

LabVIEW Software

A LabVIEW software program was written to coordinate the various parts of the CTL system. The graphical interface to this program is shown in Figure B-1.

The interface is vertically divided into three regions. The first contains controls for the motion stage. Here the user enters the GPIB address of the stepper and has the ability to set the zero position, enter a specified position, and control the stepper speed.

The second region contains controls for the scanning mirror. The position of the beam can be adjusted via the center position control. Pulse time is varied by controlling the angular deflection of the mirror according to the curve in Figure 3-3. The user can also input a test frequency that oscillates the beam about the center position. This is useful for verifying pulse time with a photodiode and oscilloscope.

The bottom third of the interface has controls used to expose a line on the wafer. The software uses the scanning mirror to swing the beam past the slit, exposing a spot for the desired amount of time. Then the program shifts the stage over by the step size, normally some significant fraction of the beam diameter, and exposes again. This process is repeated until the specified number of steps has been reached.

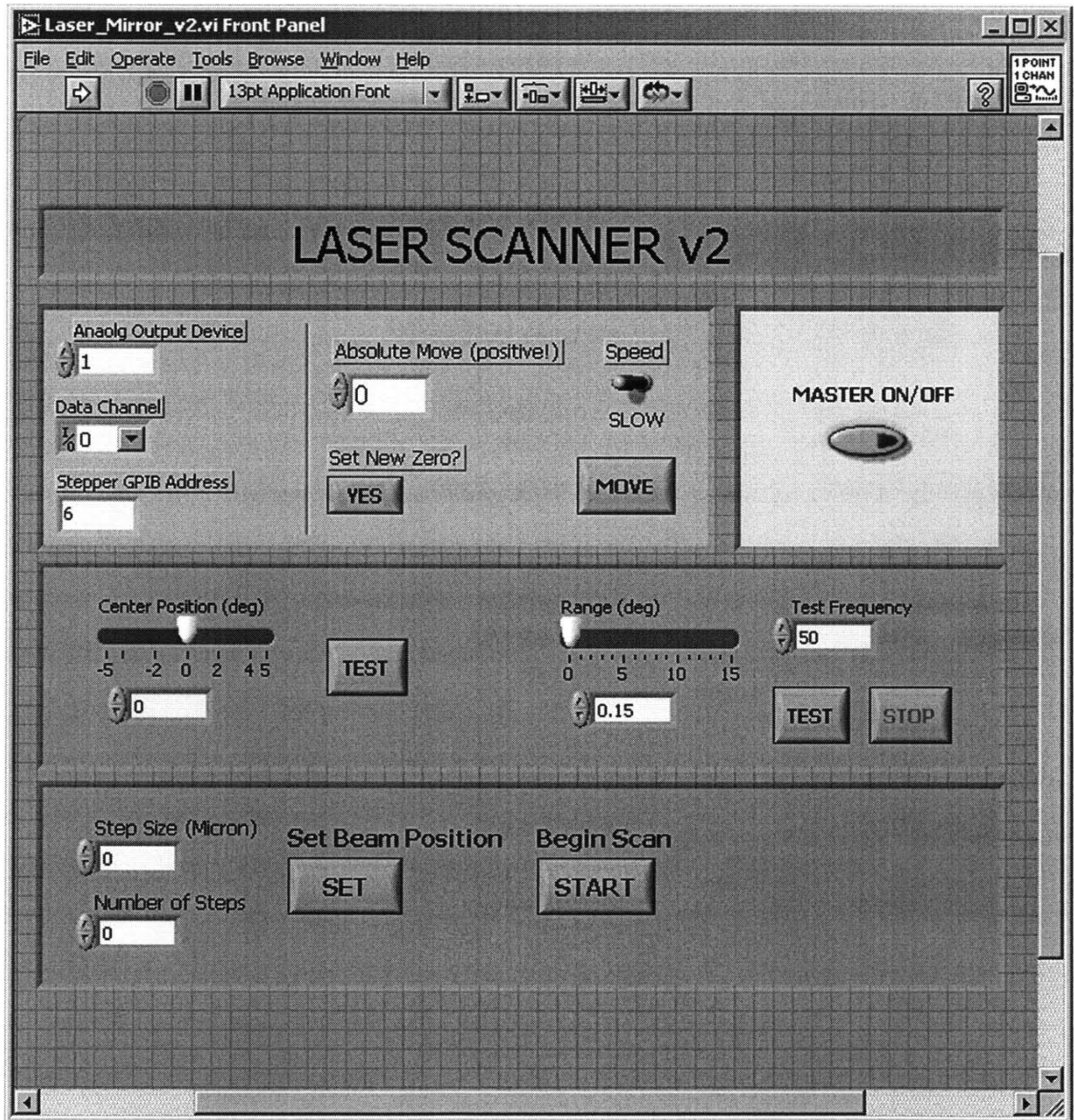

Figure B-1: LabVIEW interface for the CTL system.

Bibliography

[1] James G. Goodberlet. Patterning sub-50 nm features with near-field embedded-amplitude masks. *Applied Physics Letters*, 81(7):1315–1317, August 2002.

[2] Ed Muzio, Phil Seidel, Gil Shelden, and John Canning. An overview of cost of ownership for optical lithography at the 100 nm and 70 nm generations. *Semiconductor Fabtech*, 11:191–194, 1999.

[3] S.Y. Chou, P.R. Krauss, and P.J. Renstrom. Nanoimprint lithography. *Journal of Vacuum Science and Technology B*, 14(6):4129, 1996.

[4] Stephen Y. Chou, Peter R. Krauss, Wei Zhang, Lingjie Guo, and Lei Zhuang. Sub-10 nm imprint lithography and applications. *Journal of Vacuum Science and Technology B*, 15(6), Nov/Dec 1997.

[5] Michael D. Austin and Stephen Y. Chou. Fabrication of 70 nm channel length polymer organic thin-film transistors using nanoimprint lithography. *Applied Physics Letters*, 81(23):4431–4432, December 2002.

[6] Clivia M. Sotomayor Torres. *Alternative Lithography: Unleashing the Potentials of Nanotechnology.* Kluwer Academic Publishers, Boston, 2002.

[7] M. Colburn, S. Johnson, M. Stewart, S. Damle, T. Bailey, B. Choi, M. Wedlake, T. Michaelson, S.V. Sreenivasan, J. Ekerdt, and C.G. Wilson. Step and flash imprint lithography: A new approach to high resolution patterning. *SPIE: Emerging Lithographic Technologies III*, 3676(1):379, 1999.

[8] D.J. Resnick, T.C. Bailey, W.J. Dauksher, D. Mancini, K.J. Nordquist, E. Ainley, K. Gehoski, J.H. Baker, S. Johnson, M. Meissl, S.V. Sreenivasan, J.G. Ekerdt, and C.G. Willson. High resolution templates for step and flash imprint lithography. *Proc. SPIE*, 4688:205, 2002.

[9] M. E. Colburn. *Step and Flash Imprint Lithography: A Low-Pressure, Room-Temperature Nanoimprint Lithography.* PhD thesis, The University of Texas at Austin, 2001.

[10] Max Born and Emil Wolf. *Principles of Optics.* Cambridge University Press, United Kingdom, 7th expanded edition, 1999.

[11] G. Chen, D. Borca-Tasciuc, and R.G. Yang. *Encyclopedia of Nanoscience and Nanotechnology*, chapter Nanoscale Heat Transfer. American Scientific Publishers, in press.

[12] C. L. Choy. Thermal conductivity of polymers. *Polymer*, 18:984–1004, October 1977.

[13] K. Kurabayashi and K.E. Goodson. Impact of molecular orientation on thermal conduction in spin-coated polyimide films. *Journal of Applied Physics*, 86(4):1925–1931, August 1999.

[14] Dachen Chu, Maxat Touzelbaev, K.E. Goodson, Sergey Babin, and R. F. Pease. Thermal conductivity measurements of thin-film resist. *Journal of Vacuum Science and Technology B*, 19(6):2874–2877, November/December 2001.

[15] John H. Lienhard IV and John H. Lienhard V. *A Heat Transfer Textbook.* Phlogiston Press, Cambridge, MA, 3rd edition, 2001.

[16] James G. Goodberlet. Private communication, 2003.

[17] W. Robert Ashurst, Christina Yau, Carlo Carraro, Roya Maboudian, and Michael T. Dugger. Dichlorodimethylsilane as an anti-stiction monolayer for

mems: A comparison to the octadecyltrichlosilane self-assembled monolayer. *Journal of Microelectromechanical Systems*, 10(1):41, 2001.

[18] Bong Hwan Kim, Taek Dong Chun, Chang Hoon Oh, and Kukjin Chun. A new organic modifier for anti-stiction. *Journal of Microelectromechanical Systems*, 10(1):33, March 2001.

[19] Roya Maboudian, W. Robert Ashurst, and Carlo Carraro. Self-assembled monolayers as anti-stiction coatings for mems: characteristics and recent developments. *Sensors and Actuators*, 82:219–223, 2000.

[20] T. Bailey, B. J. Choi, M. Colburn, M. Meissl, S. Shaya, J. G. Ekerdt, S. V. Sreenivasan, and C. G. Willson. Step and flash imprint lithography: Template surface treatment and defect analysis. *Journal of Vacuum Science and Technology B*, 18(6):3572–3577, Nov/Dec 2000.

[21] Christopher B. Walsh and Elias I. Franses. Ultrathin PMMA films spin-coated from toluene solutions. *Thin Solid Films*, 429:71–76, 2003.

[22] B. J. Choi, M. Meissl, M. Colburn, T. Bailey, P. Ruchhoeft, S.V. Sreenivasan, F. Prins, S. Banerjee, J.G. Ekerdt, and C.G. Willson. Layer-to-layer alignment for step and flash imprint lithography. *Proceedings of SPIE: Emerging Lithographic Technologies V*, 4343:436, 2001.

[23] Edward D. Palik., editor. *Handbook of optical constants of solids III.* Academic Press, San Diego, CA, 1998.

[24] http://www.io.tudelft.nl/research/dfs/idemat/Onl_db/Id123p.htm, Accessed May 2004.